Experimental Study of Magnetism in Genuine Organic Radical Crystals

美藤, 正樹
Graduate School of Engineering, Kyushu University

https://doi.org/10.11501/3135018

出版情報：九州大学, 1997, 博士（工学）, 課程博士
バージョン：
権利関係：

Experimental Study of Magnetism in Genuine Organic Radical Crystals

Masaki Mito

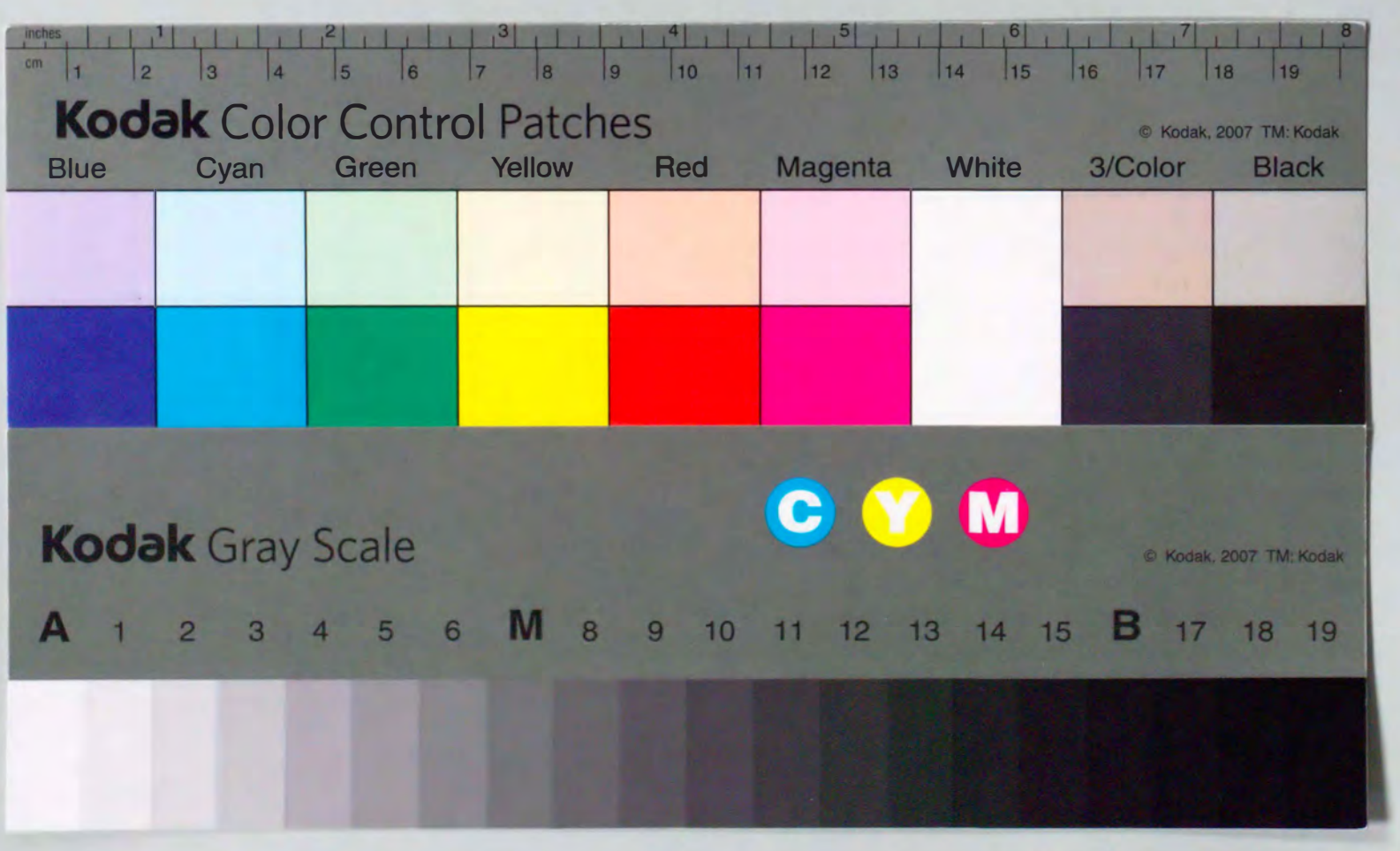

Experimental Study of Magnetism in Genuine Organic Radical Crystals

Department of Applied Physics
Faculty of Engineering
Kyushu University

Masaki Mito

January, 1998

Acknowledgement

This doctorate thesis has been completed under the guidance of Professor Kazuyoshi Takeda, and under the supervision of Professor Eisaku Miyoshi and Professor Tisato Kajiyama. The author would like to express his sincere gratitude for their support, valuable suggestions and encouragement.

The author would like to acknowledge Professor Toshihiro Idogaki for his valuable advice and for his great encouragement. The author would like to express his sincere gratitude to Dr. Tatsuya Kawae for his wholehearted supports in the experiments in the low temperature region. The author is indebted to Ms. Masako Hitaka for making the programs of experiments and her great encouragement. The author is grateful to Dr. Kensuke Konishi (Ehime University at present) and Dr. Masakazu Ito (Hiroshima University at present) for many advices in experimental techniques.

The author would like to acknowledge Professor Hiroyuki Deguchi and Professor Seishi Takagi (both at Kyushu Institute of Technology) for the measurements of magne ization and ESR, and valuable discussions.

The author would like to express his gratitude to Professor Kazuo Mukai (Ehime University) for offering such interesting samples as TOV, *p*-CDTV etc. and giving the chance to study them widely.

The author gratefully acknowledges Professor Franz A.Neugebauer (Max-Plank-Institut) for the chance to study such verdazyl series as NpTV and NDV.

The author would like to express his gratitude to Professor Minoru Kinoshita (Science University of Tokyo in Yamaguchi) and Dr. Masafumi Tamura (Toho University) for the chance to study the β-phase *p*-NPNN.

The author is indebted to Dr. Yuko Hosokoshi and Professor Katsuya Inoue (both at Institute for Molecular Science) for the chance to study such interesting samples as F_5PNN and galvinoxyl, and for the measurement of the *dc*-magnetic susceptibility under pressure.

The author gratefully acknowledges Professor Kiyofumi Nagata and Dr. Masaharu Takumi (both at Fukuoka University) for the structural analysis under pressure.

The author is indebted to Professor Kizashi Yamaguchi (Osaka University) and Dr. Mitsutaka Okumura (Osaka National Research Institute) for offering many reports and much valuable data of the theoretical calculation.

The author would like to acknowledge Professor Norio Achiwa (Kyushu University, Faculty of Science) for valuable discussions.

The author is very grateful to Mr. Shigeharu Momota and Mr. Tatsuya Ikuta for indispensable support in the experiments under pressure.

The author is very grateful to Mr. Tsutomu Soejima, Mr. Toshihiro Hotta, and

Mr. Hirotaka Ueda (Kyushu University, Faculty of Science) for the experimental supports at low temperatures.

Many thanks to the members of the laboratory of Professor Kazuyoshi Takeda, especially to Professor Yoshinori Muraoka (Ariake National College of Technology at present), Dr. Akihisa Tanaka, Dr. Milan Žukovič, Mr. Hiroaki Sakita (Advanced Display INC. at present) and Mr. Hiroyuki Nakano (Advanced Display INC. at present) for their support and valuable advice.

Contents

Chapter 1

General Introduction

The research of genuine organic ferromagnets, consisting exclusively of light elements such as H, C, N and O, has its long history since 1960s, and various experimental and theoretical strategies have been reported by many researchers in chemical fields. The discovery of first bulk-ferromagnet, β-phase para-nitrophenyl nitronyl nitroxide (hereafter abbreviated as β-*p*-NPNN), in 1991 [1] marked an epoch of the study of the magnetism of organic compounds, since it had been generally believed that almost all of radical crystals would be magnetically inactive or antiferromagnetic. At present, more than ten radical crystals are reported to be ferromagnetic, and the research for organic ferromagnet has become one of the main subjects of "molecular magnetism" which is a relatively new field involving materials science and cooperative phenomena played in quantum spin systems.

From a physical point of view, however, the characterization of magnetism of organic compounds has not been cleared, whether they are ferromagnetic or antiferromagnetic. This thesis is devoted to the experimental study of several organic radical crystals with typical magnetic properties physically understood on the basis of quantum statistics or the magneto-structural correlation. One of the highlights in this thesis is the pressure-induced ferro- to antiferromagnetic transition of β-*p*-NPNN observed for the first time in organic compounds, in chapter 6.

In this section, the author makes general remarks which are significant for the studies in the following chapters, after giving a brief remark on the recent study of organic ferromagnets.

1.1 Organic Ferromagnetic Compounds

One of the most major subjects in molecular magnetism is to realize the genuine organic bulk-ferromagnet consisting only of light elements such as H, C, N and O etc. There have been two main guiding strategies for this subject. One of them is to elevate spin multiplicity within polymers by the intramolecular or "through-bond" interactions [2]. A variety of investigations has been reported by this mean [3]. The other is to bring about ferromagnetic interactions between stacked radical molecules by the "through space" exchange interaction.

First intermolecular ferromagnetic interaction was found in galvinoxyl crystal * by Mukai *et al.* in 1967 [4]. This crystal has the ferromagnetic interaction with a large positive Weiss temperature of $\Theta = +11$ K above 85 K. However, this ferromagnetic phase changes to a nonmagnetic one at 85 K. Stimulated by this discovery, various researches for the organic bulk-ferromagnets have been activated. Eventually, it took over twenty years until a historic discovery of

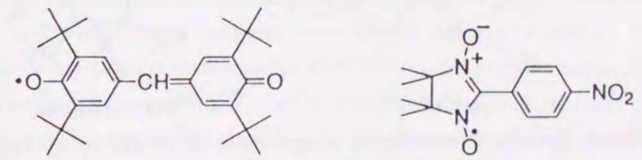

galvinoxyl p-NPNN

the first organic bulk-ferromagnet of the β-phase *p*-NPNN † by Kinoshita *et al.* in 1991 [1,5,6], although its transition temperature (T_c = 0.61 K) is fairly low for practical use. Before their reports, Awaga *et al.* have already reported the existence of the intermolecular ferromagnetic interaction ($\Theta \simeq +1$ K) and the crystal structure of this compound in 1989 [7,8]. The detailed magnetism has been investigated by the heat capacity [6], *ac*-susceptibility [6], magnetization [6], zero-field muon spin rotation (μSR) [9], neutron diffraction [10] and electron spin resonance (ESR) [11]. The magnetic easy axis has been confirmed to be the b-axis by μSR [9], neutron diffraction [10] and ESR [11]. The calculation of the magnetic dipole interaction has concluded that the magnetic dipole interaction is not the origin of the ordering, but determines the magnetic easy axis [12]. The thermal and magnetic measurements under pressure have reported the reduction of T_c by the pressure, and this result indicates that the ferromagnetism of β-*p*-NPNN originates not from the magnetic

*4-[3,5-bis(1,1-dimethylethyl)-4-oxo-2,5-cyclohexadiene-1-ylidenemethyl]-2,6-bis(1,1-dimethyl-ethyl)-phenoxyl

†para-Nitrophenyl Nitronyl Nitroxide

dipole interaction but the exchange interaction [12,13].

The intermolecular ferromagnetic interaction has been often observed in the nitronyl radical series such as *p*-NPNN, but the magnitude is generally weak because of the small delocalization of the unpaired electron: Most of the spin density concentrates on the NO-moiety. However some ferromagnetic radical crystals have been observed also in verdazyl series [14-17], in which the unpaired electron is delocalized on central four nitrogen atoms on a common plane. The *p*-CDTV [‡] has been reported to be the genuine organic ferromagnetic crystal with the strong one-dimensionality (T_c = 0.67 K) [14-16].

The genuine organic ferromagnet which has been recognized to have the highest T_c is Dupeyredioxyl [§] (T_c = 1.48 K, in 1993) [18]. However the characterization of its ferromagnetism is left unsolved, especially in the behavior of its non-hysteresis below T_c and its magnetic susceptibility around T_c.

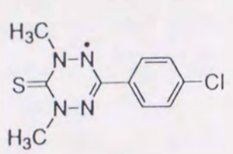

p-CDTV

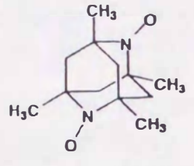

Dupeyredioxyl

Except for above introduced compounds, there are many organic ferromagnets observed until now [¶][19]. However, the transition temperature to the bulk-ferromagnetic state is generally lower than 1 K, and the characterization of their magnetism is mostly unrevealed from a physical point of view.

[‡]3-(4-chlorophenyl)-1,5-dimethyl-6-thioxoverdazyl

[§]1,3,5,7-tetramethyl-2,6-diazaadamantane-N,N'-dioxyl

[¶]for example, 4-(*p*-chlorobenzylideneamino)-2,2,6,6-tetramethylpiperidin-1-oxyl (abbreviated as TEMFO): T_c = 0.28 K [19]

1.2 General Feature of Organic Radical Molecule

Origin of Organic Magnetism The magnetism of organic radical molecules originates from the *p*-electron on molecular orbitals (MO's) occupied over entire molecule. For an allyl radical, for instance, which is one of the simplest organic radicals, there are three important molecular orbitals; NLUMO (next lowest unoccupied MO), SOMO (singly occupied MO) and NHOMO (next highest occupied MO) of Fig. 1.1. The spatial distribution of SOMO is partially localized within the molecule, and has a node on the central carbon atom. On the other hand, NLUMO and NHOMO have the delocalized distribution over entire molecule. Generally the localized SOMO is the main origin of the organic magnetic moment, and plays a dominant role to decide the intermolecular interaction, making orbital overlapping with other molecules.

Magnetic Anisotropy The organic radical crystal gives a very isotropic spin system. Generally in the inorganic ionic atoms, such as transition or rare-earth atoms, the total angular momentum ($\boldsymbol{J}$) of the orbital angular momentum ($\boldsymbol{L}$) and the spin angular momentum ($\boldsymbol{S}$) contributes to the magnetic moment $g\mu_B\boldsymbol{J}$, where g is the Lande's g-factor and $\boldsymbol{J} = \boldsymbol{L} + \boldsymbol{S}$. The quantity $\boldsymbol{L}$ couples with $\boldsymbol{S}$ through the spin-orbital interaction $\lambda\boldsymbol{L}\cdot\boldsymbol{S}$. When the orbital wave functions degenerate, the expectation-value of $\boldsymbol{L}$ or $\langle\boldsymbol{L}\rangle$ becomes non-negligible and hence it gives anisotropic g-value. However in the organic compounds consisting of light elements exclusively, the wave functions are expressed in real space independent of the time. Hence $\langle\boldsymbol{L}\rangle$ becomes zero, and the orbital angular momentum is "quenched", resulting in a very isotropic g-value contributed only from the unpaired electron spin (g = 2.0023). Therefore an organic magnet is considered as the isotropic (Heisenberg) spin system, and becomes one of the best model systems for the many-body problems of quantum statistics [‖].

[‖]The experimental results of one-dimensional (1D) organic magnets such as γ phase *p*-NPNN [6], *p*-CDTV [15,16], *p*-CDpOV [17], and DMTzNC-TCNQ [20] etc. have been compared with the theory of the S =1/2 one-dimensional Heisenberg system.

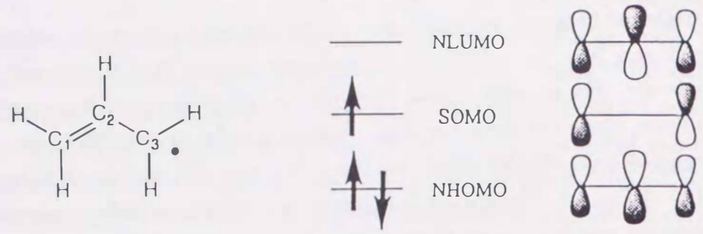

Figure 1.1: Molecular structure of allyl radical and spatial distribution of three molecular orbitals such as NLUMO (next lowest unoccupied MO), SOMO (single occupied MO) and NHOMO (next highest occupied MO).

1.3 Intermolecular Interaction

We introduce the importance of the molecular orbital (MO) overlap and the spin polarization for the spin alignment in organic magnets.

Effect of Orbital Overlap At first, we explain that it is necessary for realization of the parallel spin alignment to suppress the direct orbital overlap between SOMO's, in reference to the spin state of H_2 molecule.

Let us consider the molecular orbital of H_2 molecule in the following Hamiltonian,

$$\mathcal{H}\psi = \epsilon\psi \quad , \tag{1.1}$$

where ψ is a MO function, and ϵ is an energy level of ψ. Here two different MO functions (ψ_1 and ψ_2) are expressed by the linear combination of two atomic orbitals,

$$\text{bonding MO} : \psi_1 = \frac{\chi^{\mathrm{A}} + \chi^{\mathrm{B}}}{\sqrt{2 + 2S_{\mathrm{AB}}}} \quad , \tag{1.2}$$

$$\text{antibonding MO} : \psi_2 = \frac{\chi^{\mathrm{A}} - \chi^{\mathrm{B}}}{\sqrt{2 - 2S_{\mathrm{AB}}}} \quad , \tag{1.3}$$

where χ^{A} (χ^{B}) stands for the atomic orbital function of hydrogen atom A (B) and S_{AB} ($S_{\mathrm{AB}} \leq 1$) for the overlap integral between χ^{A} and χ^{B} as,

$$S_{\mathrm{AB}} = \int \chi_{\mathrm{A}}\chi_{\mathrm{B}} d\tau \quad . \tag{1.4}$$

Above each MO has the following energy level, respectively,

$$\epsilon_1 = \int \psi_1 \mathcal{H} \psi_1 d\tau = \frac{\alpha + \beta}{2 + 2S_{\mathrm{AB}}} \quad , \tag{1.5}$$

$$\epsilon_2 = \int \psi_2 \mathcal{H} \psi_2 d\tau = \frac{\alpha - \beta}{2 - 2S_{\mathrm{AB}}} \quad , \tag{1.6}$$

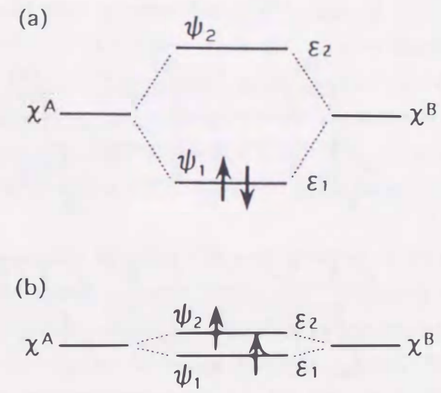

Figure 1.2: Energy levels of bonding orbital MO (ψ_1) and antibonding one (ψ_2) in two cases of large S_{AB} (a) and small one (b).

where the Coulomb integral α and the resonance one β are defined as,

$$\alpha = \int \chi^{\mathrm{A}} \mathcal{H} \chi^{\mathrm{A}} d\tau = \int \chi^{\mathrm{B}} \mathcal{H} \chi^{\mathrm{B}} d\tau \quad , \tag{1.7}$$

$$\beta = \int \chi^{\mathrm{A}} \mathcal{H} \chi^{\mathrm{B}} d\tau \quad , \tag{1.8}$$

and both integrals have negative values in the case of H_2. The energy gap ($\Delta\epsilon$) between ϵ_1 and ϵ_2 becomes

$$\Delta\epsilon = \epsilon_1 - \epsilon_2 = \frac{\beta - \alpha S_{\mathrm{AB}}}{1 - S_{\mathrm{AB}}^2} \quad . \tag{1.9}$$

For a large S_{AB}, $\Delta\epsilon$ becomes negative and ϵ_1 becomes more stable than ϵ_2 as Fig. 1.2.(a).

In this case, eventually, the antiparallel spin alignment is realized according to the Hund's rule. On the other hand, for a smaller S_{AB}, $\Delta\epsilon$ becomes much smaller, resulting in the parallel spin alignment from the Hund's rule as Fig. 1.2.(b). Then the relation between energy splitting and spin arrangement can be expressed in the spin space with the exchange interaction ($2J^{\mathrm{AB}} \equiv \Delta\epsilon$) in the following Heisenberg-type of Hamiltonian,

$$\mathcal{H} = -2J^{\mathrm{AB}} S^{\mathrm{A}} \cdot S^{\mathrm{B}} \quad , \tag{1.10}$$

where S^{A} (S^{B}) is the total spin operator for atom A (B).

Next we extend this problem to the case of allyl radical [21]. Figure 1.3 shows three types of stacking modes, in which only SOMO is considered. φ_+ and φ_- stand for the bonding and antibonding combinations between two SOMO's, respectively.

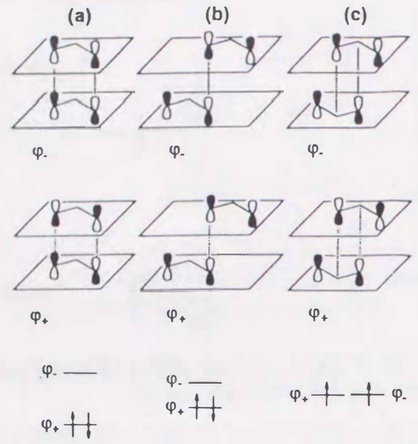

Figure 1.3: Orbital interactions in the magnetic coupling of two allyl radicals.

In the stacking modes (a) and (b), overlap is not zero; therefore the wave function φ_+ is stabilized and φ_- is destabilized. The SOMO-SOMO overlap in mode (a) is larger than that in mode (b), and therefore the energy splitting in mode (a) should be larger than that in mode (b). On the other hand, the SOMO-SOMO overlap in the stacking mode (c) almost vanishes. A semiquantitative discussion of the orbital orthogonality indicates that the node of SOMO on the central carbon plays an great role in the cancellation of the practical overlap. The energy splitting in mode (c) is therefore nearly zero. As a result the triplet state is possible, following the Hund's rule. Thus the control of molecular arrangement is necessary for creating the ferromagnetic intermolecular coupling.

Effect of Spin Polarization In 1963 McConnell suggested, considering the effect of spin polarization (SP) within a molecule, that the "through space" exchange interaction between two aromatic radicals could be approximated by the following Heisenberg Hamiltonian,

$$\mathcal{H}^{AB} = -\sum_{ij} 2J_{ij}^{AB} S_i^A \cdot S_j^B = -S^A \cdot S^B \sum_{ij} 2J_{ij}^{AB} \rho_i^A \rho_j^B \quad , \tag{1.11}$$

where J_{ij}^{AB} is an exchange integral between atom i of molecule A and atom j of molecule B, S_i^A (S_j^B) is the electron spin density on atom i (j) of molecule A (B),

S^A (S^B) is the total spin operator for A (B), and ρ_i^A (ρ_i^B) is a spin density on atom i (j) of molecule A (B), respectively [22]. Above Hamiltonian mentions the following physics: Since J_{ij}^{AB} (evaluated in the context of valence bond theory) is usually negative, the effective exchange interaction between two radicals can be ferromagnetic if the spin-density product $\rho_i^A \rho_i^B$ ($i \neq j$) is negative. One of the experimental checks of this model is examined in carbenic dimers, for example **.

Extended McConnell's Model Yamaguchi *et al.* extended this McConnell's model to more generalized magnetic system [23]. Generally the orbital overlap of singly occupied molecular orbitals (SOMO's) between free radicals is predominant in the decision of the effective exchange integrals J_{ab}, and that contribution brings about the negative (antiferromagnetic) J_{ab}. On the other hand, the computational experiment suggests that the spin polarization (SP) effect induces the possibility to bring about the positive (ferromagnetic) J_{ab}. In this extended McConnell's model (EMM), therefore, the nearest neighbor effective exchange integral J_{ab}(EMM) for radical clusters is given as follows:

$$J_{ab}(\mathrm{EMM}) = J_{ab}(\mathrm{OO}) + J_{ab}(\mathrm{SDP}) \quad , \tag{1.12}$$

where J_{ab}(OO) is the orbital term depends on the SOMO-SOMO overlap, and J_{ab}(SDP) is the spin density term according to,

$$J_{ab}(\mathrm{SDP}) = J(\mathrm{SDP}) \sum_i \rho_i(\mathrm{A})\rho_i(\mathrm{B}) \quad , \tag{1.13}$$

where ρ_i(Y) is the spin density at a site i of molecule Y(=A,B) as illustrated in Fig. 1.4, and J(SDP) has a negative value. The sign of J_{ab}(OO) is generally negative all the time. But J_{ab}(SDP) may have a positive value if a value of $\sum_i \rho_i(\mathrm{A})\rho_i(\mathrm{B})$ is negative (because of $J(\mathrm{SDP}) < 0$). That is to say, according to this EMM, the ferromagnetic exchange integral (positive J_{ab}(EMM)) can be brought about, when a magnitude of positive J_{ab}(SDP) overcomes that of negative J_{ab}(OO). It is necessary for positive J_{ab}(EMM) to minimize the SOMO-SOMO overlap and, furthermore, make the product of the spin density negative.

by A.Izuoka, H.Iwamura *et al.*: J.Am.Chem.Soc.107**(1985)1786.

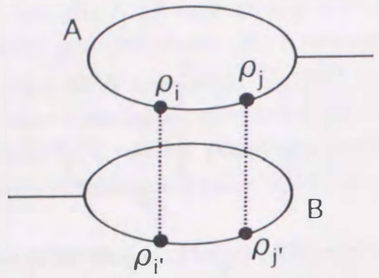

Figure 1.4: Spin densities (ρ_j) induced by the spin polarization effect, which are responsible for the spin-density-product (SDP) term.

1.4 Ferro- and Antiferro-Magnetic Interactions and Molecular Stacking

In addition to the exchange interactions treated in the previous section, here we mention another mechanism for realizing parallel spin alignment by introducing the concept of the charge transfer (CT) between molecular orbitals (MO's).

In 1987 Awaga *et al.* introduced the charge transfer model to explain the ferromagnetic intermolecular interaction in galvinoxyl radical crystal known to have ferromagnetic interaction [24,25], and stressed the importance of indirect or superexchange interaction in addition to the direct SOMO-SOMO interaction. Generally the CT interaction, which is common in organic solids, is observed even in the crystals of free radicals [26]. This CT model is based on the spin-unrestricted picture, where α (up) spin and β (down) spin occupy different orbitals by the effect of spin polarization.

Generally the magnetic interaction J^{AB} between molecules A and B is expressed as

$$J^{AB} = J_P^{AB} + J_K^{AB} \quad , \tag{1.14}$$

where J_P^{AB} stands for the potential interaction and J_K^{AB} for the kinetic one to which we refer here. The potential exchange (J_P^{AB}) originates directly from the MO's overlap determined mainly by the crystal structure, in which the minimization of SOMO-SOMO overlap is the great condition for the parallel spin alignment as mentioned in previous section. On the other hand, the kinetic exchange (J_K^{AB}) originates from the CT, and its effect is divided into mainly two types; (a) the direct CT between SOMO and SOMO, and (b) the indirect one via other MO (*e.g.* NHOMO).

In the case (a) of Fig. 1.5, the CT between α-SOMO of molecule A and β-SOMO of molecule B stabilizes the singlet configuration, and then the kinetic interaction

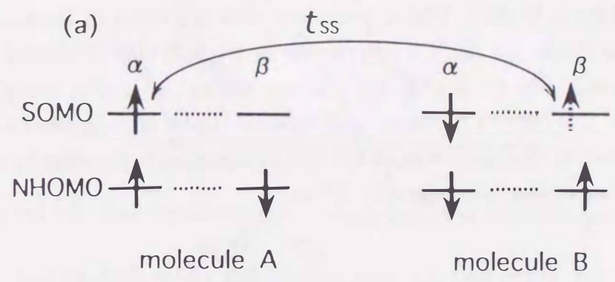

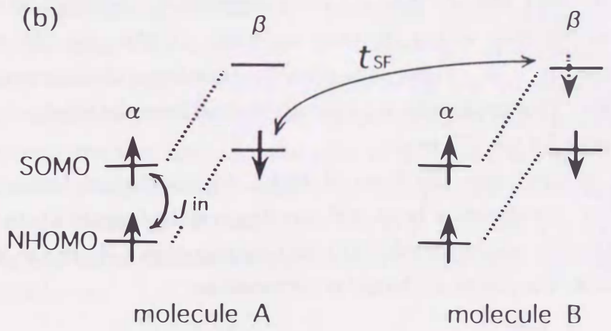

Figure 1.5: Charge transfer (CT) between molecule A and molecule B; (a) possible configuration for CT between SOMO and SOMO, and (b) that for CT between SOMO and NHOMO. α and β stand for the up-spin and the down-spin, respectively. t_{SS} is the CT between SOMO's, t_{SF} is the CT between SOMO and a fully occupied MO (*e.g.* NHOMO), and J^{in} is the intramolecular exchange integral between SOMO and NHOMO within the same molecule.

($J_{\mathrm{K}}^{\mathrm{AB}}$) is expressed in the antiferromagnetic form as

$$J_{\mathrm{K}}^{\mathrm{AB}} = -\frac{t_{\mathrm{SS}}^2}{U} \quad , \tag{1.15}$$

where t_{SS} stands for the CT integral between SOMO's and U for the on-site Coulomb repulsion in SOMO. This is consistent with the result of the second order perturbation theory for the CT interaction in the half-filled Hubbard Hamiltonian. In the case of Fig. 1.5.(b), the CT between the highest doubly occupied β-NHOMO of A and β-SOMO of B occurs, and then the triplet configuration is realized between SOMO and NHOMO in molecule A with orthogonal symmetry or small overlapping, resulting in the ferromagnetic $J_{\mathrm{K}}^{\mathrm{AB}}$ as

$$J_{\mathrm{K}}^{\mathrm{AB}} = \frac{t_{\mathrm{SF}}^2}{U^2} J^{\mathrm{in}} \quad , \tag{1.16}$$

where t_{SF} stands for the CT integral between SOMO and a fully occupied MO (*e.g.* NHOMO), and J^{in} does for the intramolecular exchange integral between SOMO and NHOMO within the same molecule. In this case, J^{in} is positive within the molecule. This process ends when the transferred β-electron returns to the original state. This mechanism is physically derived from the third order of the perturbation theory for the CT model.

In conclusion, the direct SOMO-SOMO interaction brings about the AFM coupling. On the other hand, FM coupling may be brought about mainly from SOMO-NHOMO and/or SOMO-NLUMO overlappings. From the discussion mentioned above, the kinetic exchange is expressed as

$$\begin{aligned} J_{\mathrm{K}}^{\mathrm{AB}} = & -\frac{t_{\mathrm{SS}}^2}{U} + \frac{t_{\mathrm{SF}}^2}{U^2} J^{\mathrm{in}} \\ & + (\text{terms related to other paths}) \quad . \end{aligned} \tag{1.17}$$

We illustrate this model, quoting the example of galvinoxyl radical. In the galvinoxyl radical crystal, the SOMO orbital has its maximum amplitude at both ends of the molecule, and the molecular arrangement with the nearly minimum SOMO-SOMO overlap as shown in Fig. 1.6 is realized. The SOMO-SOMO overlap at three central carbon atoms is supposed to be suppressed by the existence of the node as in Fig. 1.3.(c), and the potential exchange $J_{\mathrm{P}}^{\mathrm{AB}}$ supports the parallel spin alignment. But the magnitude of this potential exchange is not enough to explain the experimental fact, and the kinetic exchange must be taken into account as an indispensable effect.

Figure 1.7 shows the π-MO energy arrangement of galvinoxyl near the SOMO level by INDO calculations [24,25]. The level of NHOMO-β is higher than that of

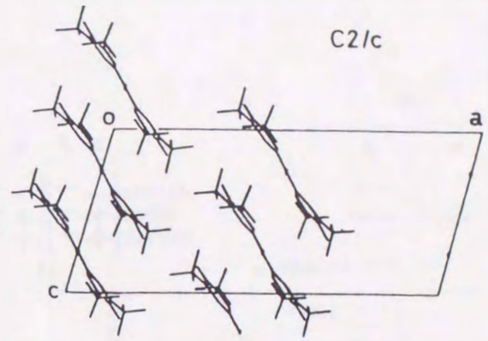

Figure 1.6: The crystal structure of galvinoxyl at room temperature.

SOMO-α, and the MO energy arrangement is of the type of Fig. 1.5.(b). Thus the ground state of galvinoxyl is expected to become ferromagnetic.

Next Fig. 1.8 shows that of *p*-NPNN [25]. The fourth HOMO-β maintains higher energy than SOMO-α, as is the same as the case of galvinoxyl. The charge density in SOMO is mostly concentrated on two NO-moieties in Fig. 1.9. Accordingly, it is expected that the SOMO-SOMO overlap is minimized provided that the NO-moieties of neighboring radicals do not approach each other in the crystal as Fig. 1.10. On the other hand, the charge distribution of other orbitals ranges over the whole molecule. Hence the overlap between SOMO and other MO (*e.g.* NHOMO and NLUMO) is expected to become large. These are quite favorable for the ferromagnetic interaction, as discussed above.

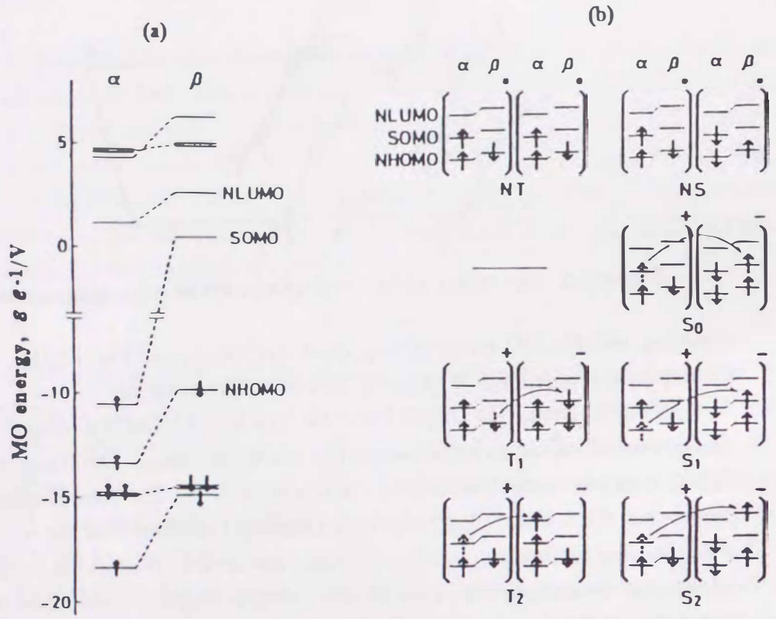

Figure 1.7: (a) The π-MO energy arrangement of galvinoxyl near the SOMO level. The α- spin orbitals and the corresponding β-spin orbitals are connected with dotted line. (b) The electronic configurations in the radical pair coupled by the CT interaction. NS and NT are the no-bond structures of singlet and triplet multiplicities. S_i and T_i are the excited singlet and triplet CT state configurations. Among the excited CT configurations, S_0 realized by the CT from α-SOMO to β-SOMO in the separate radicals is a lowest configuration. The resonance between T_1 and NT stabilizes a triplet state, whereas that between S_1 and NS results in the stabilization of the singlet state. The resonance (the configuration interaction) between S_0 and NS stabilizes the singlet state, resulting in an antiferromagnetic (AFM) interaction. However the stabilization of NS by an admixture of S_0 is expected to be minimized from quite a small SOMO-SOMO overlap. On the other hand, T_1 and T_2 must be lower in energy than S_1 and S_2, respectively. In fact, the large spin polarization, that is, the large splitting between the α- and β-spin levels in NHOMO and NLUMO suggests that T_1 and T_2 are much stabilized with respect to S_1 and S_2. The admixture of NT with T_1 and T_2 results in the stabilization of the triplet state, and the effect is expected to outweigh that of NS.

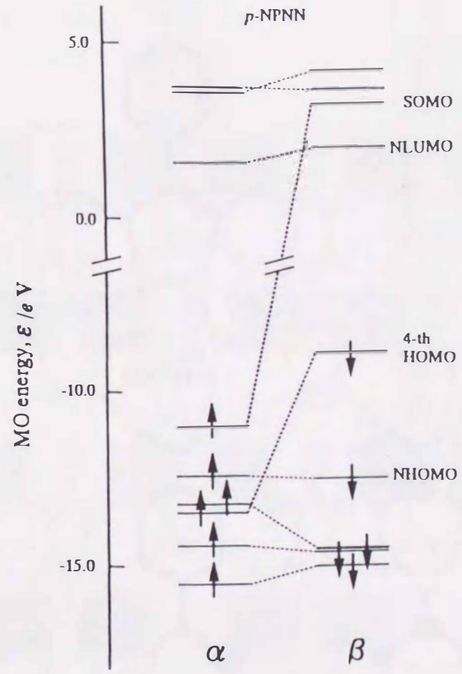

Figure 1.8: The MO energy arrangement of *p*-NPNN

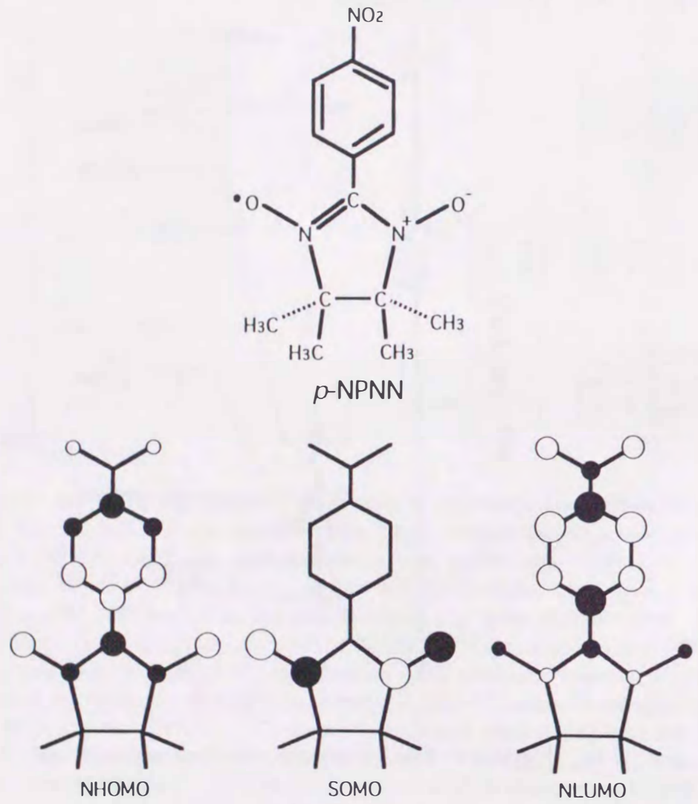

Figure 1.9: Spatial distribution of three frontier orbitals within a *p*-NPNN molecule [27].

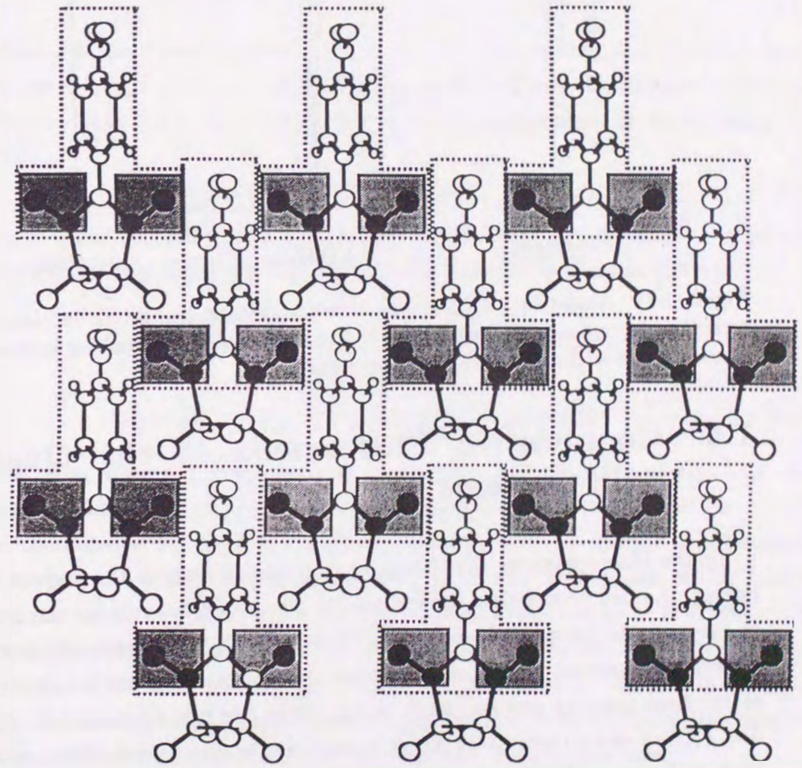

Figure 1.10: Spatial distribution of some π orbitals on the ac-plane of *p*-NPNN crystal [27]. The region painted out expresses the SOMO's distributed one. The region enclosed with the dotted line expresses that by the other MO's (NHOMO and/or NLUMO).

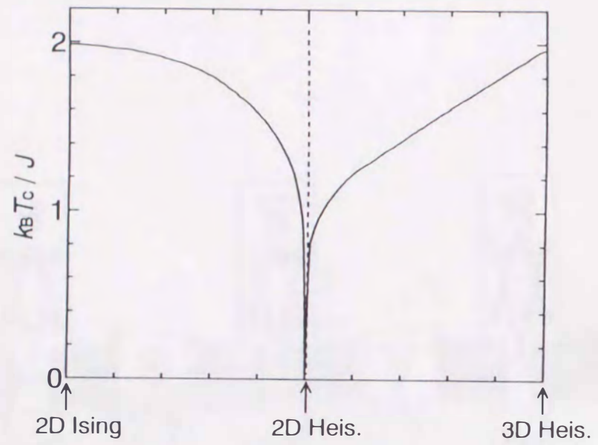

Figure 1.11: Anisotropy dependence of ordering temperature T_c and interlayer interaction dependence of one in the two-dimensional (2D) Heisenberg system [30]. T_c is normalized with the exchange interaction J.

1.5 Cooperative Phenomena in the Quantum Spin Systems

In the ideal quantum Heisenberg spin system, to which the organic magnets belong, the magnetic lattice dimensionality plays a crucial role for the occurrence of the magnetic long range order [28]. There is a magnetic order only in the three dimensional system, and then singularity appears in the physical quantities such as the heat capacity and magnetic susceptibility. In a low-dimensional system as one- (1D) or two-dimensional (2D) systems, only the broad peak reflecting the short range order is seen [28,29]. However, the introduction of a slight magnetic anisotropy and/or weak interchain or interlayer interactions induce the magnetic order even in the low-dimensional system [30]. Figure 1.11 shows the appearance of magnetic order in the cases where the 2D Heisenberg system shifts to the 2D Ising one with the increasing magnetic anisotropy, and to the 3D Heisenberg system with the increasing interlayer interaction. This indicates the peculiarity of 2D Heisenberg system for the magnetic ordering.

Here we mention two cooperative phenomena expected in the quantum spin systems, which will be examined experimentally in the following chapters.

Magnetic Field Effect Applying an external magnetic field is an effective method to discriminate whether the compound belongs to the ferromagnetic system or the antiferromagnetic one. Here we illustrate a dimer system of $S = 1/2$ Heisenberg spin, where two spins (S_1 and S_2) interacts with the exchange interaction (J) each other under a external magnetic field H, and the Hamiltonian is defined as

$$\mathcal{H} = -2JS_1 \cdot S_2 + g\mu_B H(S_{1z} + S_{2z}) \quad , \tag{1.18}$$

where g is the Lande's g-factor, μ_B is the Bohr magneton, and S_{1z} (S_{2z}) stands for the z-component of S_1 (S_2). The eigenstates of this Hamiltonian in the zero magnetic field ($H = 0$) are expressed by linear combinations of the following four states,

$$\alpha(1)\alpha(2),\ \alpha(1)\beta(2),\ \beta(1)\alpha(2),\ \beta(1)\beta(2), \tag{1.19}$$

where α and β stand for the up-spin and the down-spin, respectively. The relation between the eigenvalue (E) and the eigenfunction (Ψ) is listed as follows:

$$E_1 = -\frac{1}{2}J\ , \quad \Psi_1 = \begin{cases} \alpha(1)\alpha(2) \\ (1/\sqrt{2})(\alpha(1)\beta(2) + \beta(1)\alpha(2)) \\ \beta(1)\beta(2) \end{cases} \quad , \tag{1.20}$$

$$E_2 = \frac{3}{2}J\ , \quad \Psi_2 = \frac{1}{\sqrt{2}}(\alpha(1)\beta(2) - \beta(1)\alpha(2)) \quad . \tag{1.21}$$

The order of energy levels depends on the sign of J as shown in Fig. 1.12. The positive (ferromagnetic) J stabilizes the triplet state Ψ_1 with E_1, and the negative (antiferromagnetic) one does the singlet state Ψ_2 with E_2. Even a small magnetic field splits the triplet state as shown in Fig. 1.12, and the influence of this splitting appears in the thermodynamic quantity. Actually this magnetic field effect is remarkably seen in the 1D Heisenberg ferromagnetic radical crystals [15-17]. Figure 1.13 shows the field dependence of magnetic heat capacity reflected in p-CDpOV [17]. On the other hand, the antiferromagnetic system is insensitive to the magnetic field, indicating the magnetic field independence of the singlet state.

Dimerization Effect We mention the dimerization in the 1D Heisenberg system. In Fig. 1.14, we show some general 1D systems; the uniform chain (a) where each spin on the chain is magnetically coupled by an uniform exchange interaction J, and nonuniform chain systems such as the dimer chain (b) and the alternating one (c). Three cases of Fig. 1.14.(a-c) respectively correspond to (a) $\alpha = 1$, (b) $\alpha = 0$, and (c) $0 < \alpha < 1$ in the following Heisenberg Hamiltonian,

$$\mathcal{H} = -2\sum_{i}^{N/2}(J_1 S_{2i-1} \cdot S_{2i} + J_2 S_{2i} \cdot S_{2i+1}) \quad , \tag{1.22}$$

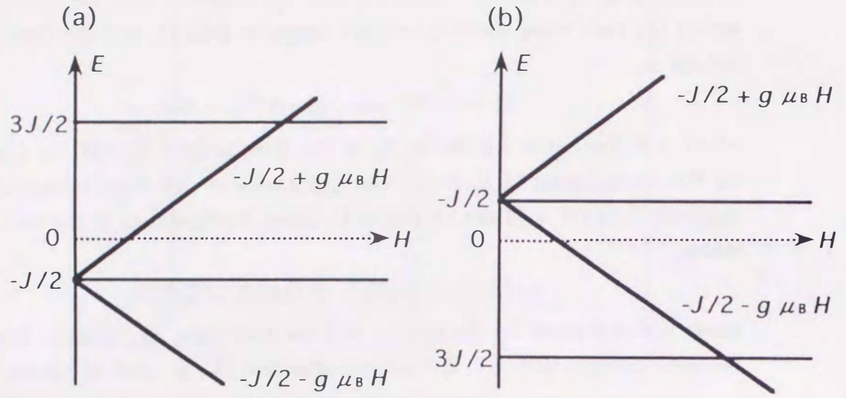

Figure 1.12: Energy level of the dimer system of $S = 1/2$ in such two case as ferromagnetic ($J > 0$; a) and antiferromagnetic ($J < 0$; b).

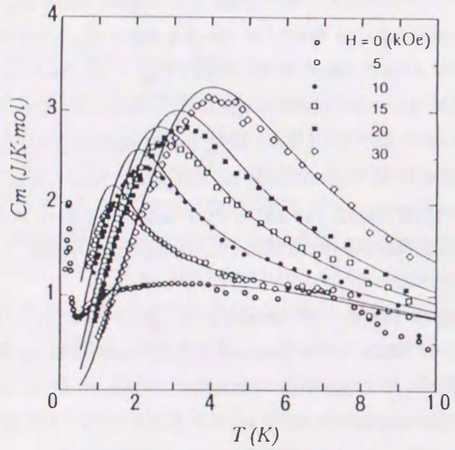

Figure 1.13: Magnetic field dependence of the magnetic heat capacity of p-CDpOV crystal [17]. The solid lines are the theoretical results for the $S = 1/2$ 1D ferromagnetic system.

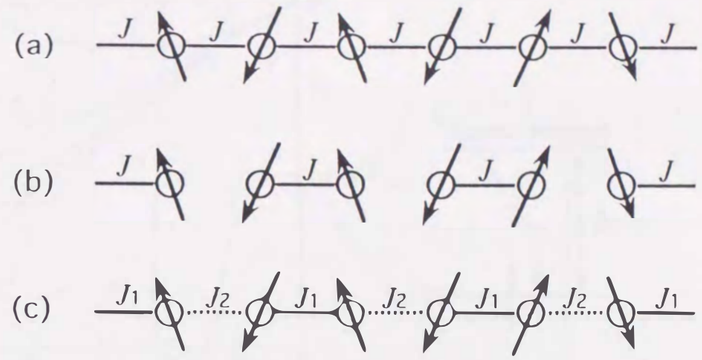

Figure 1.14: (a) Uniform chain system, (b) dimer one, and (c) alternating one. Open circles stand for the Heisenberg spin. J, J_1, and J_2 express exchange interactions between nearest spins.

where α stands for the alternating ratio (i.e. $\alpha = |J_2/J_1|$, $|J_1| > |J_2|$), and N is the number of spin. In above three cases, thermodynamic properties differ largely, depending on the energy gap (Δ) between the ground state (E_0) and the first excited state (E_1). Figure 1.15 shows α dependence of Δ in the 1D Heisenberg AF chain [31]. The cases of (b) and (c) have the finite Δ, but the uniform chain (a) does not. This fact causes the difference of temperature dependences of heat capacity ($C_{\rm H}$) and magnetic susceptibility (χ) as shown in Fig. 1.16. The former cases have the exponential initial gradient against the temperature in $C_{\rm H}$ and χ, reflecting the finite Δ. However, the uniform chain (a) has the linear initial gradient of $C_{\rm H}$ and the finite value of χ at $T \to 0$, reflecting non-energy-gap in the system. We can discriminate the system by investigating the thermodynamic properties of these physical quantities at low temperatures.

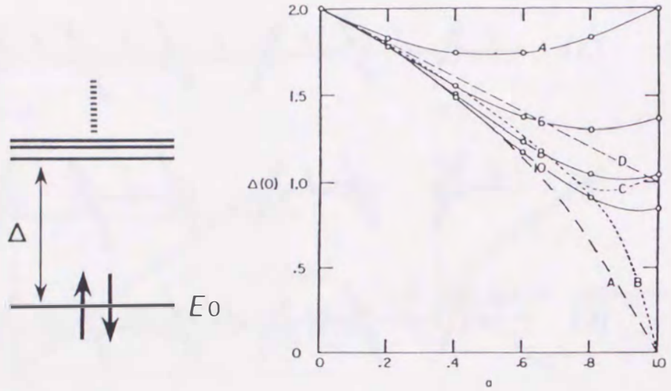

Figure 1.15: α dependence of energy gap (Δ) in the 1D Heisenberg AF chain [31]. E_0 stands for the energy of the ground state. (o) The Duffy *et al.*'s calculations for $N = 4$, 6, 8, and 10 [31], (A) the Bulaevskiĭ's Hartree-Fock result [32], (B) the Montgomery's quasiboson calculation [33], (C) the Soos's pseudospin calculation [34], and (D) the triplet exciton gas calculation by Lynden-Bell and McConnell [35].

1.6 Constitution of This Thesis

The purpose of this doctorate thesis is to make the underlying mechanism of organic molecule-based magnetism clear from a physical aspect. The contents will be mainly divided into the following three subjects:

(1) to verify and/or elucidate the mechanism which produces the intermolecular ferromagnetic and antiferromagnetic interactions in organic molecule-based magnets from a physical aspect (**chapter 3 – 9**);

(2) to examine the experimental results of the thermodynamic and magnetic properties of the organic magnets with the quantum statistical theories in various magnetic lattice dimensionality or molecular stacking (**chapter 3, 4, and 7 – 8**);

(3) to investigate the magneto-structural correlations in exchange coupled systems by introducing the magnetic anisotoropy and the pressure in organic molecule-based magnets with the isotropic spin and mechanically the soft crystal structure (**chapter 4 – 9**).

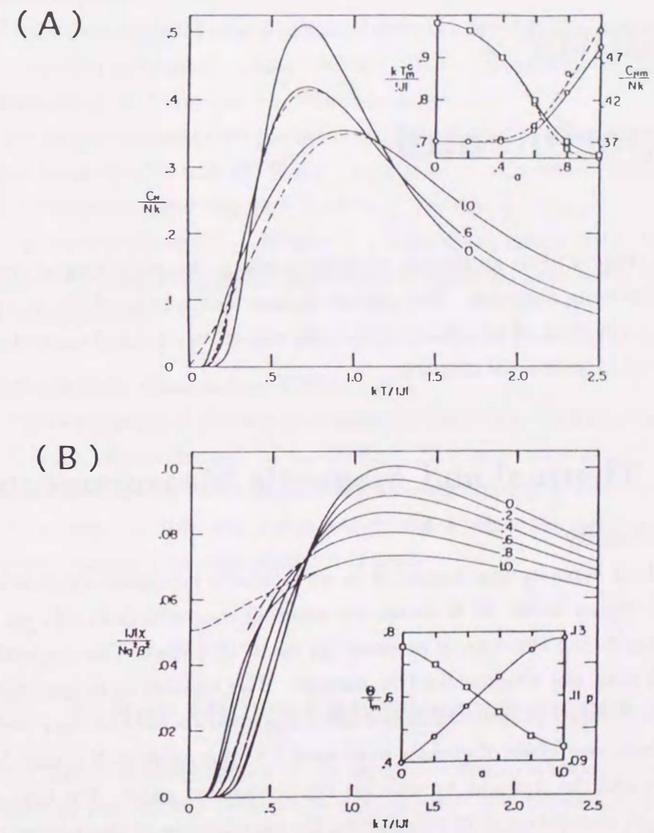

Figure 1.16: α dependence of heat capacity (C_{H}; A) and magnetic susceptibility (χ; B) in the 1D Heisenberg AF alternating chain [31]. The dashed curves are the estimates for $N = \infty$. The data for $\alpha = 1.0$ is the result by Bonner and Fisher [36]. (A): C_{H} of the 10-spin chain for $\alpha = 0$, 0.6 and 1.0. The inset shows the temperature of the maximum $kT_{\mathrm{m}}/|J|$ (o) and the value of the maximum C_{Hm}/Nk ($\Box$) vs α. (B): χ of the 10-spin chain for $\alpha = 0$, 0.2, 0.4, 0.6, 0.8 and 1.0. The inset shows the Weiss constant divided by the temperature of the maximum Θ/T_{m} (o) and the product of the maximum times the corresponding temperature, $p = \chi_{\mathrm{m}} kT_{\mathrm{m}}/Ng^2\beta^2$ ($\Box$) vs α.

Chapter 2

Experimental

This chapter gives an overall description about the experimental methods used in the following chapters. The organic radical compounds which we treat in this thesis are synthesized in collaboration with respective chemical researchers, and are mentioned in individual chapters.

2.1 Thermal and Magnetic Measurements

Heat Capacity

The heat capacity was measured by an adiabatic heat-pulse method in the temperature region below 40 K under the external magnetic field (H) up to 30 kOe and/or under the hydrostatic pressure (p) up to 10.4 kbar. The magnetic field was supplied with the superconductive magnet. The method of pressurization of the sample is detailed in section 2.3. For attaining good thermal contact within sample compounds, two kinds of greases were used, i.e. the Apiezon-N grease (at ambient pressure) and the Apiezon-J grease (at the pressurized state). The heat capacity of the sample was obtained by subtracting the contribution of the addenda (i.e. thermometer, heater, Cu platform, Apiezon-N grease etc.) from the observed total heat capacity.

Ac Magnetic Susceptibility

The *ac*-magnetic susceptibility above 1.7 K was measured by the Hartshorn bridge method with the Lakeshore 7110 AC Susceptometer, which was operated for the *ac*-field (H_{ac}) up to 10 Oe (peak-to-peak) at the frequency (f) up to 1 kHz. The measurement of *ac*-susceptibility at lower temperatures ($T \leq 2.0$ K) was performed by the Hartshorn bridge method with the NF 5610B two phases lock-in amplifier ($H_{ac} = 0.6$ Oe (peak-to-peak) and $f = 100$ Hz) or by utilizing the *ac*-resistance

bridge method ($H_{ac} = 0.1 \sim 1.0$ Oe (peak-to-peak) and $f = 15.9$ Hz: LR-700 *ac*-resistance bridge) . The maximum value of H is 10 kOe in this case.

Magnetization

The measurement of magnetization (M) up to $H = 50$ kOe above 1.7 K was performed with the Quantum Design MPMS SQUID magnetometer (Kyushu Institute of Technology and Institute for Molecular Science).

The magnetization under the small magnetic field (100 Gauss) in the temperature region between 4.2K and 150 K was also measured with the HOKUSAN HSM 2000 SQUID magnetometer (Kyushu University, Faculty of Science).

The magnetization ($M - H$) curve in lower temperature region below 0.5 K was obtained by integrating the *ac*-susceptibility, which corresponds to $\mathrm{d}M/\mathrm{d}H$, against the external field.

Electron Spin Resonance (ESR)

The experiment of electron paramagnetic resonance (EPR) absorption spectrum at X-band was performed by a standard ESR spectrometer (JEOL JES-RE2X: Kyushu Institute of Technology) in the temperature region between 1.4 K and 290 K. The magnetic field was calibrated by the NMR tesla meter and by the quite isotropic standard material with $g = 2.0023$.

2.2 X-Ray Diffraction Measurements

For the structural analysis of the sample compounds under pressure, the X-ray diffraction pattern was obtained by a Rigaku RU-300 diffractomoter with an imaging plate (Fukuoka University), where Mo-K_α radiation ($\lambda = 0.710$ Å) was used. The diffraction pattern was analyzed by the Rietveld method [37] to estimate lattice constants.

2.3 Pressurization Methods

Depending on the physical quantities and the temperature ranges, the following two methods were used to realize the pressurized state; (1) **the clamp cell method** and (2) **the diamond anvil method**.

Clamp Cell Method

The heat capacity, magnetic susceptibility, and magnetization under pressure were measured by using the following three types of Cu-Be clamp cells [13,38,39].

The first type of Cu-Be clamp cell (Fig. 2.1.(A)) was used in the experiments shown in chapters 7, 8 and 9. The pressure-transmission was attained by the Apiezon-J grease, which also worked effectively for the thermal contact. In this method, the sample was compressed at room temperature and clamped with the locking nut (Fig.2.1.(a)). The real value of pressure at low temperatures was calibrated with the pressure dependence of the superconductive transition temperature $T_s(p)$ of Sn [40], In [40], or Pb [41], which was set in the sample room. Figure 2.2 shows the relation between the real pressure at liquid ^{4}He temperature and the load applied at room temperature in the Cu-Be clamp cell of Fig. 2.1.(A).

The second type (Fig. 2.1.(B)) with the same structure as the first one (Fig. 2.1.(A)) was used in the experiments for the higher pressure as in chapter 6. The Apiezon-K grease, whose viscosity is larger than that of the Apiezon-J grease, was used as the pressure transmission oil. The real pressure at low temperatures was estimated in the same way as the first type (Fig.2.2), and a tip of metallic aluminum (Al) was set in the cell as the superconductive metal for the pressure calibration. For reference, the pressure dependence of $T_s(p)$ of Al has the following approximate relation [42],

$$\frac{dT_s}{dp} = -2.9 \pm 0.2 \text{ K}/10^2\text{kbar} \quad . \tag{2.1}$$

These representative results are shown in Fig. 2.3, which were detected by the ac-magnetic susceptibility.

The last type (Fig. 2.4) was planned to get the high pressure compactly, and was used in the experiment of chapter 5. The inner diameter was shrunk down to 4 mm to produce higher pressure: The sample, the pressure transmission oil (Apiezon-K grease) and Al were enclosed in the teflon cell to prevent the pressure from leaking. The limited value of applied pressure in this type is about 13.0 kbar against the load of 130 kgf/cm^2.

Diamond Anvil Method

The pressure for the X-ray diffraction experiment was realized with the diamond anvil cell at room temperature. The fluorine oil was used for the pressure transmission, and the real pressure was estimated by the Ruby fluorescence in this method. The standard wavelength (λ) of the red R_1 fluorescence of Ruby (Al_2O_3: 0.5% Cr) shifts toward the long wavelength with the increasing pressure up to 200 kbar [43] as

$$\frac{d\lambda}{dp} = 0.3634 \pm 0.0005 \text{ Å/kbar} \quad , \tag{2.2}$$

where $\lambda(p = 0) = 6422.4$ Å at the ambient pressure. The wavelength under each pressure was determined by averaging λ's from three pieces of Ruby, which were placed near the sample.

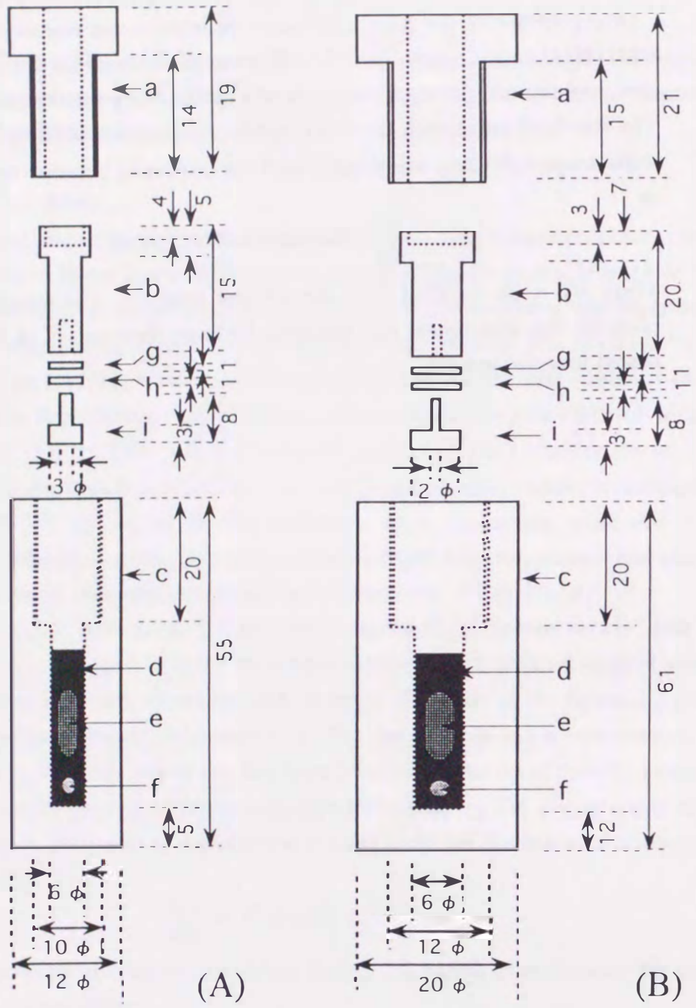

Figure 2.1: Cross-sectional view of first two types of Cu-Be clamp cells. (a) Locking nut, (b) piston, (c) cylinder, (d) pressure transmission oil, (e) sample, (f) superconductive metal, (g) Cu seal, (h) teflon seal, and (i) mushroom plug.

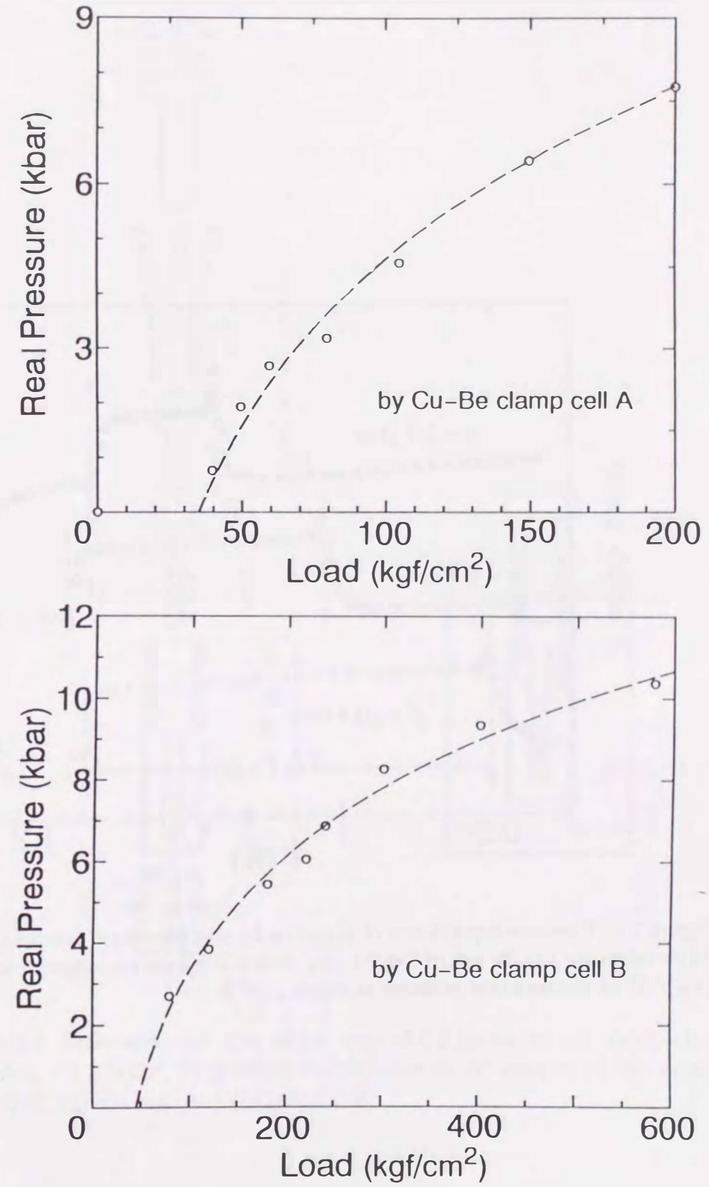

Figure 2.2: Relation between the real pressure at liquid ^{4}He temperature and the load applied at room temperature in two types of Cu-Be clamp cells of Fig.2.1. The broken lines are guides for the eye.

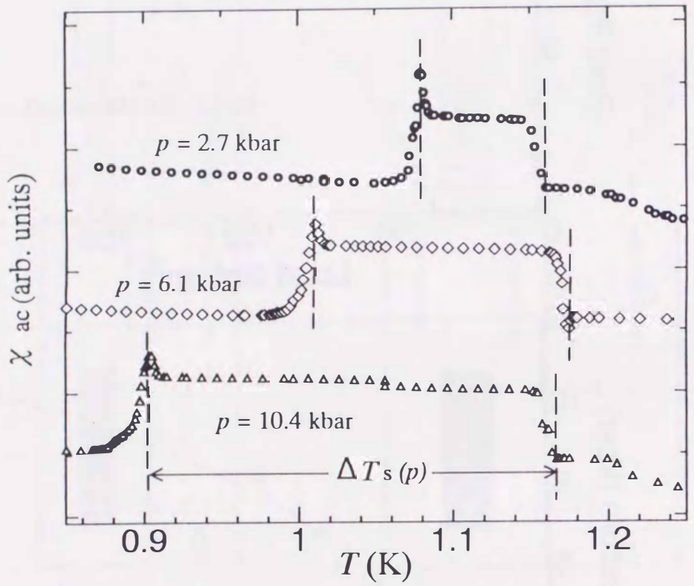

Figure 2.3: Pressure dependence of superconductive transition temperature $T_s(p)$ of Al metal in the Cu-Be cell of Fig.2.1.(B), detected by the *ac*-magnetic susceptibility (χ_{ac}). T_s at the ambient pressure is about 1.17 K.

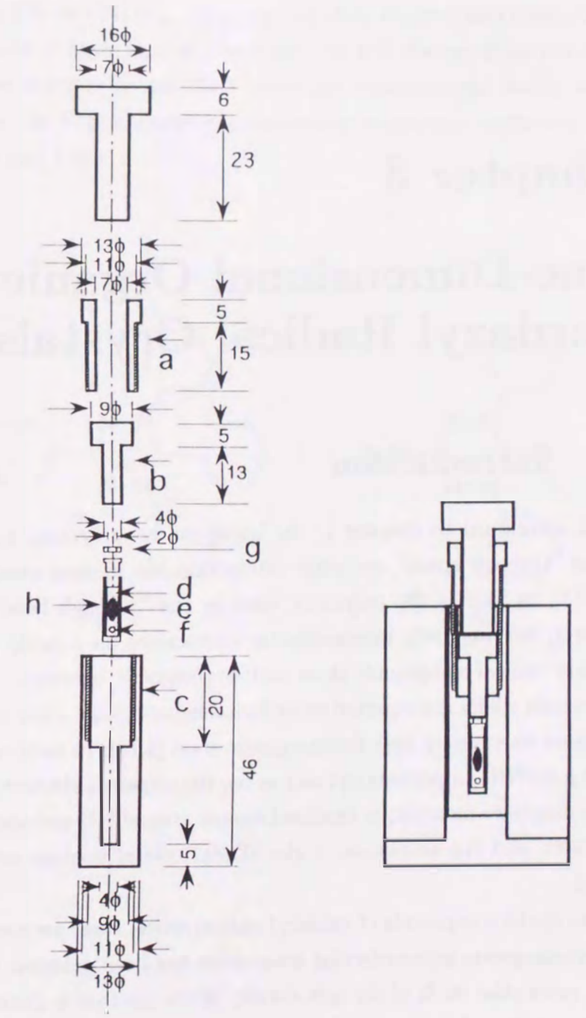

Figure 2.4: Cross-sectional view of last type of Cu-Be clamp cell. (a) Locking nut, (b) piston, (c) cylinder, (d) pressure transmission oil, (e) sample, (f) superconductive metal (Al), (g) Cu seal, and (h) teflon cell.

Chapter 3

One-Dimensional Organic Verdazyl Radical Crystals

3.1 Introduction

As mentioned in chapter 1, the quest for nonpolymeric organic ferromagnets by the "through space" exchange interaction has uprisen among recent ten years [1,14,18], as well as the polymeric ones by the "through bond" interactions [2,3]. However, ferromagnetic intermolecular interactions have rarely been realized, while ordinary radical compounds show antiferromagnetic behavior. Even in the organic compounds which are reported to be ferromagnetic, only a few compounds show the transition to a purely bulk-ferromagnetic state [1,18]. In such radical crystals as β-phase *p*-NPNN, Dupeyredioxyl and so on, the unpaired electron, which is the origin of the magnetic moment, is localized almost around NO-moieties in the constituent molecules, and the amplitude of the SOMO orbital is quite large near the radical moiety.

Also in the compounds of verdazyl radical series, there are some crystals in which the ferromagnetic intermolecular interaction has been detected [14-17] * †. In these cases, more than 90 % of the spin density of the electron is distributed on the plane of the central verdazyl moiety [44] ‡. Therefore we expect to get much clear information about the relation between intermolecular interaction and crystallized molecular arrangement, considering the molecular orbitals. All of four nitrogen atoms at the verdazyl ring are reviewed on a plane as seen in the following section, and this fact makes it easier to speculate the orbital overlapping in the crystal. This chapter reports the magnetic properties of two 1,5-diphenylverdazyl radical crystals (abbreviated as NpTV and NDV). By analyzing their thermal and magnetic properties and the results of their crystal structures, we will discuss from the experimental point of view whether or not their molecular arrangements satisfy the necessary condition for the ferromagnetic intermolecular interaction explained in chapter 1 (sections 1.3 and 1.4).

*[14-16]: 3-(4-chlorophenyl)-1,5-dimethyl-6-thioxoverdazyl (*p*-CDTV)
†[17]: 3-(4-chlorophenyl)-1,5-diphenyl-6-oxoverdazyl (*p*-CDpOV)
‡See Fig.4.2

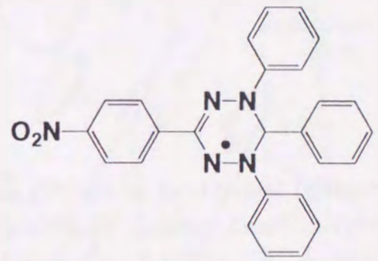

NpTV

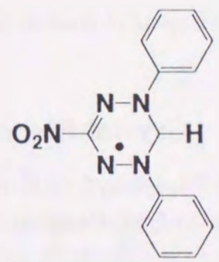

NDV

3.2 Experimental Results and Discussion of NpTV

The crystal structures of both compounds have recently determined in detail [45]. The calculation of molecular orbitals (MO's) is being undertaken on the topological information by Prof. Mukai *et al.*, from which the knowledge of the spin polarization and the energy level of each MO will be deduced. Prio to these theoretical calculations, in this chapter we represent the experimental results of magnetic measurements on these crystals, and discuss the intermolecular interactions considering the overlapping of possible MO's in the crystals.

3.2.1 Crystal Structure

3-(4-Nitrophenyl)-1,5,6-triphenylverdazyl (abbreviated as NpTV) crystal was prepared by Prof. Neugebauer's group (Max-Planck-Institut). The crystal structure belongs to triclinic (P_1^-) with a = 6.596 Å , b = 12.755 Å , c = 13.160 Å , α = 87.24 °, β = 84.16 ° and γ = 83.90 ° [45] as shown in Fig. 3.1. Generally in the verdazyl derivatives, the SOMO is localized around the co-planer nitrogens of the verdazyl ring as will be mentioned in chapter 4 [44]. The verdazyl ring with the large positive spin density population at four nitrogens is in contact with the adjacent coplanar 4-nitrophenyl segment bearing very small positive and negative spin density population (Fig. 3.1.(b)). Consequently the dominant overlapping of MO's is expected along the stair-like path as shown in Figs. 3.1.(b) and (c) with quite a small SOMO-SOMO overlap compared with the overlap between SOMO and other MO's (*e.g.* NHOMO). Such molecular arrangement is similar to that of β-*p*-NPNN (Fig.1.10), and hence the ferromagnetic intermolecular interaction can be expected along the stair-like molecular stacking in the NpTV crystal.

3.2.2 Magnetic Susceptibility

The *ac*-magnetic susceptibility (χ_{ac}) in the temperature region between 1.8 K and 100 K was measured by utilizing the Lakeshore 7110 AC Susceptometer (H_{ac} = 10 Oe (peak-to-peak), f = 125 Hz), where the sample mass (m) was 45.1 mg. χ_{ac} between 0.67 K and 5.8 K was measured by the LR-200 *ac*-resistance bridge (H_{ac} = 0.1 Oe (peak-to-peak), f = 15.9 Hz) where m = 317.9 mg. The experimental result was corrected for the diamagnetic contribution of χ_{dia} = -0.241 × 10^{-3} emu/mol by

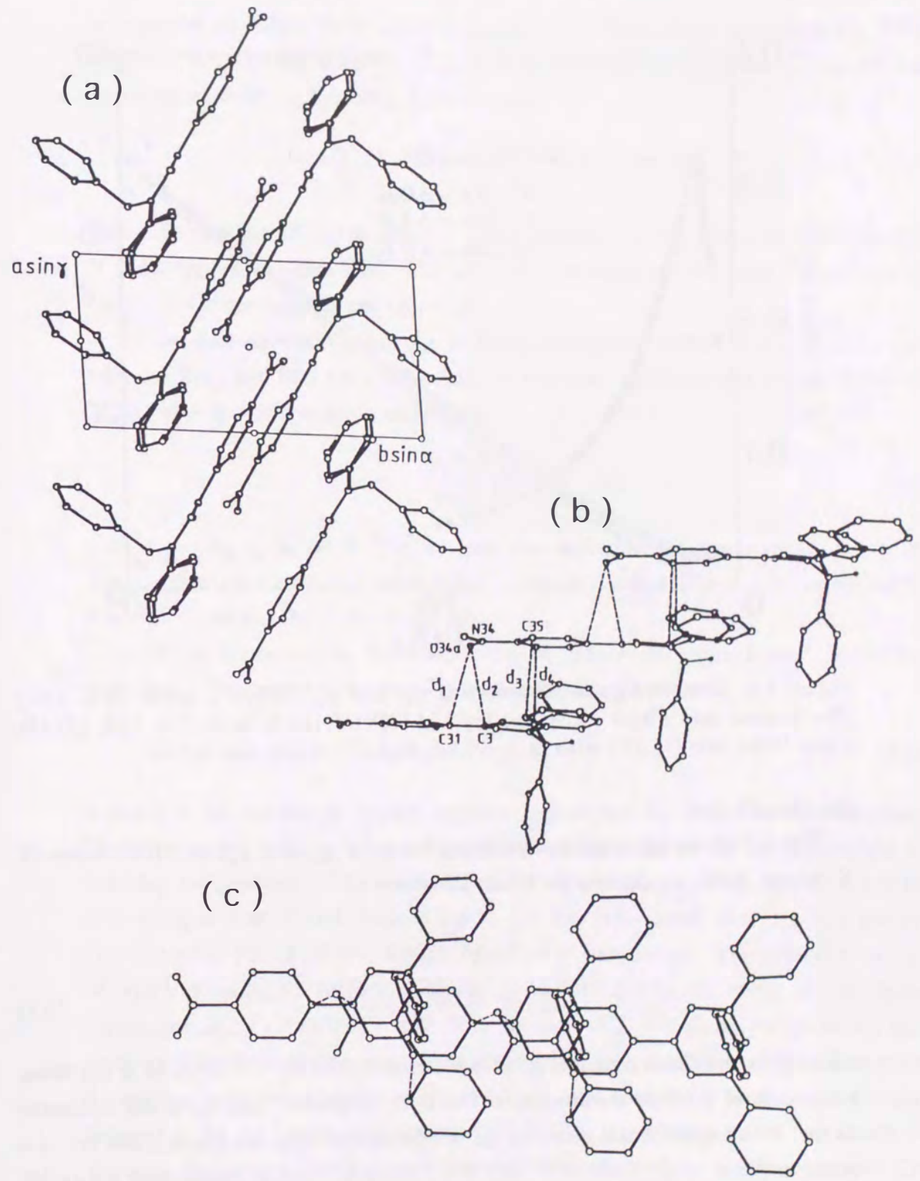

Figure 3.1: (a)Crystal structure of NpTV viewed along the *c*-axis. (b) Crystal stacking of NpTV in a side view showing the stair-pattern and the intermolecular overlap between adjacent molecules. Shortest intermolecular distances between the adjacent verdazyl ring and the 3(4-nitrophenyl) substituent: d_1(O34a-C31^i)=3.372 Å , d_2(O34a-C3^i)=3.381 Å , d_3(C35-C16^i)=3.369 Å , d_4(C33-N5^i)=3.398 Å [symmetry code i; 1+x,y,z]. (c) View onto the verdazyl N1,N2,N4,N5 plane of NpTV showing the side-shift of the chain.

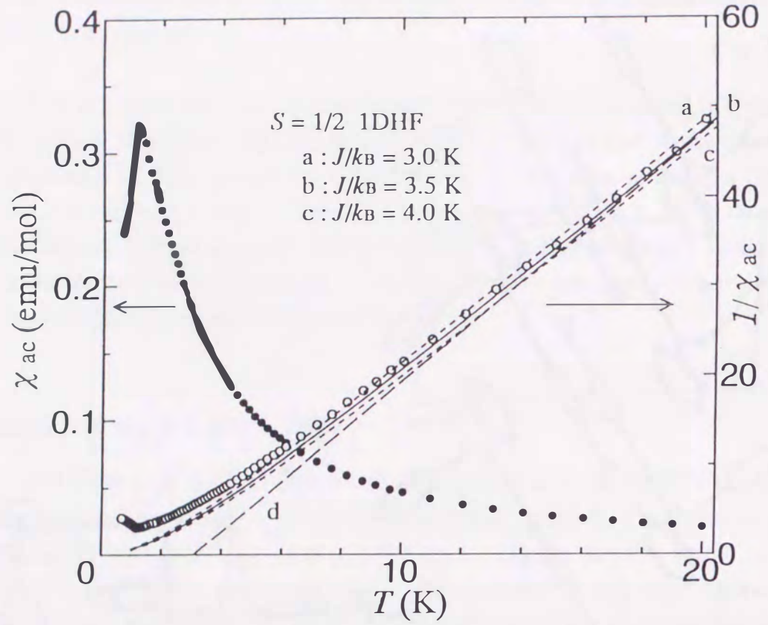

Figure 3.2: Temperature dependences of χ_{ac} and χ_{ac}^{-1} of NpTV below 20 K. (a-c) The Bonner and Fisher's theories (*eq*.3.3) [36] for 1DHF with $S = 1/2$, (d) the Curie-Weiss law (*eq*.3.1) with $\Theta = +3.1$ K and $C = 0.358$ emu·K/mol.

the Pascal's law.

Fig. 3.2 shows the temperature dependences of χ_{ac} and χ_{ac}^{-1} of NpTV below 20 K. Above 20 K, χ_{ac} follows the Curie-Weiss law

$$\chi = \frac{C}{T-\Theta} \quad , \qquad C = \frac{g^2\mu_B^2 S(S+1)}{3k_B} \quad , \tag{3.1}$$

where C is the Curie constant ($C = 0.375$ emu·K/mol for $S = 1/2$), Θ is the Weiss temperature, g is the g-value, μ_B is the Bohr magneton, and k_B is the Boltzman factor. The experimental result of χ_{ac} is reproduced with the Curie-Weiss law of a positive Weiss temperature $\Theta = +3.1 \pm 0.2$ K and $C = 0.358$ emu·K/mol, indicating the existence of the ferromagnetic interaction between neighboring molecules, as we have speculated in subsection 3.2.1. The positive value of Θ in this compound has been also reported by Allemand *et al*.[46].

As described in the previous subsection 3.2.1, the crystal structure of NpTV

is expected to belong to a one-dimensional (1D) Heisenberg ferromagnetic (HF) system. Therefore the behavior of χ_{ac} may be analyzed on the quasi-1D Heisenberg ferromagnet with the following Hamiltonian,

$$\mathcal{H} = -2J\sum_i S_i \cdot S_{i+1} - 2J'\sum_{i\neq j} S_i \cdot S_j - g\mu_B H\sum_i S_i^z \quad , \tag{3.2}$$

where J and J' are the intra- and interchain exchange interactions, respectively, and H is an applied external field. The value of J' is much smaller than J, but acts to trigger the three-dimensional ordering.

As the first approximation, χ_{ac} in the paramagnetic region is dominantly contributed from the first term in *eq*.3.2. In the case, the magnetic susceptibility of 1DHF with $S = 1/2$ is given as follows,

$$\chi_{1D} = \frac{Ng^2\mu_B^2}{4k_BT}\{1 + (\frac{J}{k_BT})^a\} \quad , \tag{3.3}$$

with $a = 1$ for $k_BT/J > 1$ [36]. In fact, the experimental results of χ_{ac} below 20 K are reproduced by *eq*.3.3 with $J/k_BT = 3.5 \pm 0.5$ K and $g = 2.00$, as shown in Fig. 3.2, deviating the Curie-Weiss law.

At lower temperatures, the effect from the interchain interaction J' has to be considered. The mean field theory gives the following relation,

$$k_BT_N \cong 2S^2\sqrt{|\, zJ' \cdot J\,|} \quad , \tag{3.4}$$

where z is the number of nearest neighbor chains, and T_N is the three-dimensional (bulk) magnetic ordering temperature (which is also available for the ferromagnetic ordering temperature). The ratio of J and J' is estimated to be $|\, J'/J\,| \cong 0.1$ with $z = 4$, $T_N = 1.16$ K and $J/k_B = 3.5$ K. On the other hand, the Oguchi's theory [47] estimates $|\, J'/J\,| \cong 0.05$ for the same set of parameters. The deviation of χ_{ac} of NpTV from *eq*.3.3 below 5.0 K will be mainly due to the effect of interchain interaction of $|\, J'/J\,| \cong 0.05 \sim 0.1$. Now the sign of J' is definitely negative by the analysis of low temperature susceptibilities as follows; χ_{ac} continues to increase with decreasing temperature down to $T_N = 1.16$ K, and then turns to decrease sharply below T_N. At the lowest temperature $T = 0.67$ K, χ_{ac} reaches about two thirds of maximum value of χ_{ac}, as seen in the susceptibility of powdered antiferromagnets: In the mean field theory for the bulk-antiferromagnet below the ordering temperature (T_N; Néel temperature), the powdered susceptibility (χ_{powder}) is shown as follows,

$$\chi_{powder} = \frac{1}{3}\chi_{//} + \frac{2}{3}\chi_{\perp} \quad , \tag{3.5}$$

where $\chi_{//}$ and $\chi_{\perp}$ are the parallel and the perpendicular susceptibilities, respectively. Below $T_{\rm N}$, $\chi_{//}$ decreases toward zero, but $\chi_{\perp}$ is constant. Hence at the temperature zero,

$$\chi_{\rm powder}(T=0) = \frac{2}{3}\chi_{\perp}(T=0) \quad . \tag{3.6}$$

This suggests that the NpTV crystal undergoes the bulk-antiferromagnetic transition at $T_{\rm N} = 1.16$ K.

3.2.3 Heat Capacity

Heat capacity of the powdered sample of NpTV ($m = 317.9$ mg) mixed with the Apiezon-N grease ($m = 291.8$ mg) has been measured in the temperature region between 0.73 K and 20 K, under the external fields of $H = 0$, 480 and 1530 Oe. Figure 3.3 shows the experimental results of heat capacity ($C_{\rm p}$) under the zero field. A distinct peak, which is concerned with three-dimensional order observed by the *ac*-susceptibility measurement, is detected at $T_{\rm N} = 1.10$ K being followed by a flat plateau at higher temperatures above $T_{\rm N}$.

The magnetic heat capacity $C_{\rm m}$ is evaluated from $C_{\rm p}$ by subtracting the lattice heat capacity ($C_{\rm lattice}$). For lack of a non-magnetic and isostructured radical compound for $C_{\rm lattice}$, here the lattice contribution is approximated with the Debye function,

$$\begin{aligned} C_{\rm lattice} &= r \times 3Nk_{\rm B}f_{\rm D}(x) \quad , \\ f_{\rm D}(x) &= 3x^{-3}\int_0^x \frac{e^y y^4}{(e^y-1)^2}dy \quad , \end{aligned} \tag{3.7}$$

in which the lattice vibration is treated as the elastic wave of the continuous elastic body: r is the effective number of atomic groups vibrating in the unit cell, and $f_{\rm D}(x)$ is the Debye function with $x = \Theta_{\rm D}/T$ ($\Theta_{\rm D}$; Debye temperature). On the other hand, the total magnetic entropy $S_{\rm m}(T=\infty)$ for N-spins of the spin-value S should approach toward $Nk_{\rm B}ln(2S+1)$ theoretically, where $S_{\rm m}(T)$ is expressed as

$$\begin{aligned} S_{\rm m}(T) &= \int_0^T \frac{C_{\rm m}}{T}dT \quad , \\ C_{\rm m} &= C_{\rm p} - C_{\rm lattice} \quad . \end{aligned} \tag{3.8}$$

For the best fit between these relations and the experimental results of NpTV, $\Theta_{\rm D}$ and r are estimated to be $\Theta_{\rm D} = 71$ K and $r = 2$, respectively. Figure 3.3 shows the temperature dependence of $S_{\rm m}$, whose lower part is estimated under the assumption of $Cm \propto T^3$ for the three-dimensional spin wave theory ($T < 0.73$ K). The lower

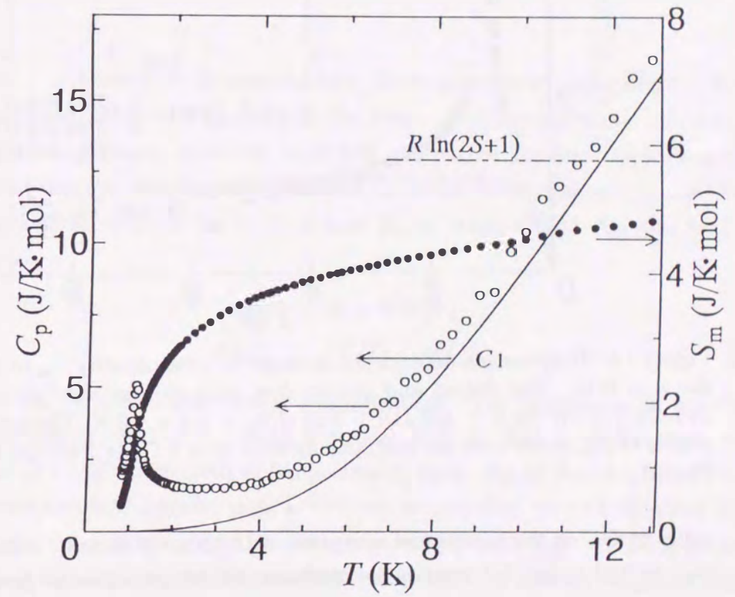

Figure 3.3: Temperature dependence of heat capacity $C_{\rm p}$ (o) of NpTV under the zero field below 13 K. The solid line expresses the lattice contribution which is the Debye function (*eq*.3.7) with $\Theta_{\rm D} = 71$ K and $r = 2$. The closed circles (•) express the magnetic entropy $S_{\rm m}$.

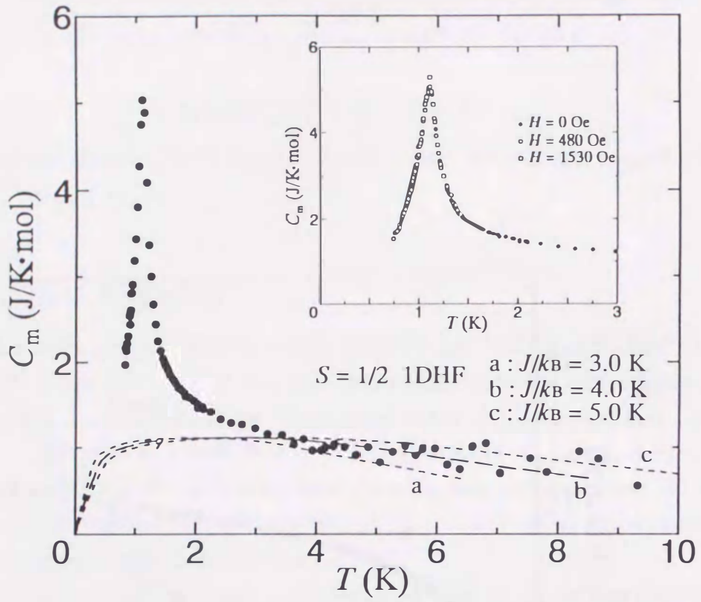

Figure 3.4: Temperature dependence of magnetic heat capacity C_m of NpTV under the zero field. The dotted and broken lines (a-c) express the Takahashi *et al.*'s theories [48] for the $S = 1/2$ 1DHF with $J/k_B = 4.0 \pm 1.0$ K. The inset shows the results of C_m under such the magnetic fields as $H = 0$ Oe (•), 480 Oe (○) and 1530 Oe (□).

value of Θ_D of this compound compared with those of metallic substances (*e.g.* $\Theta_D \simeq 320$ K for Cu) implies the mechanically soft structure of genuine organic compounds.

The intrinsic magnetic heat capacity (C_m) of NpTV is shown in Fig. 3.4. It is noted that the plateau of C_m is reproduced by the Takahashi *et al.*'s theory [48] for the $S = 1/2$ 1DHF with $J/k_B = 4.0 \pm 1.0$ K in which,

$$\frac{C_{max}}{Nk_B} \simeq 0.134 \quad , \tag{3.9}$$

$$\frac{k_B T_{max}}{|J|} \simeq 0.70 \quad , \tag{3.10}$$

where C_{max} stands for the maximum value of C_m, and T_{max} corresponds to the temperature at which C_{max} appears. If the magnetic interaction of this system is antiferromagnetic with the same absolute value J, much larger value (about three times) of C_{max} is theoretically expected, as will be given for the next NDV compound. The sharp peak at $T_N = 1.10$ K is stable even in the external fields up to 1.53 kOe as seen in the inset of Fig. 3.4. The field independence of the peak makes a good contrast to the sensitive field dependence in the bulk-ferromagnet β-phase *p*-NPNN, where the sharp peak becomes round with about a half height of its maximum peak value even in the magnetic field of 0.15 kOe [6]. Rather the behavior of NpTV under the external fields shows a general feature of antiferromagnets in the external fields, and resembles the case of the bulk-antiferromagnet γ-phase *p*-NPNN [6].

-note- Generally in the external field, the magnetic heat capacity peak shows a characteristic behavior depending on the ferro- or antiferromagnetic interaction of the system. However, there are small field and narrow temperature regions where the heat capacity is independent of these variables: When the system has the net magnetization $M(T)$ in the external field H, the internal field H_{int} and $M(T)$ are given as

$$\begin{aligned} H_{int} &= H - NM(T) \quad , \\ M(T) &= M_s(T) + \chi(T)H \quad , \end{aligned} \tag{3.11}$$

where $M_s(T)$ is the spontaneous magnetization. The application of a small H induces $M(T)$, and there exists a critical field H_c and a temperature region ($\Delta T = |T - T_c|$, T_c; the critical temperature), where H_{int} is canceled to be zero. In this case, the heat capacity peak is almostly independent of the field below H_c. In the case of β-*p*-NPNN, $H_c \approx 100$ Oe is reported [6]. Above $H > H_c$, the change of the heat capacity peak is characterized by the ferro- or antiferromagnetic interaction of the system. When the temperature is approached to its ordering temperature (T_c), the ferromagnet has fairly large local moments while in the antiferromagnet the singlet pairing of spins is developed with much smaller net moments. This is a qualitative explanation of the field independence of the heat capacity peak of NpTV in such a high field $H = 1530$ Oe $\gg H_c$ as in Fig. 3.4. When the external field increases toward the interchain exchange field $H = 2z|J'|\langle S\rangle/g\mu_B \approx 12$ kOe, the heat capacity peak is expected to shift toward lower temperatures.

3.2.4 Conclusion of NpTV

The results of χ_{ac} and C_m indicate that NpTV is approximated as an $S = 1/2$ quasi-1D Heisenberg ferromagnet with the intrachain ferromagnetic exchange con-

stant J/k_B = 4.0 ± 1.0 K, and the interchain antiferromagnetic one J'/k_B = -0.4 ± 0.1 K, by which the whole system orders three-dimensionally at $T_N \cong$ 1.1 K. This fact is qualitatively understood by considering the crystal structure as seen in Fig.3.1, where the SOMO-SOMO overlap along the chain is very small and larger orbital overlap between SOMO and other MO (*e.g.* NHOMO) can be expected. However, as seen in Fig.3.1.(a), neighboring ferromagnetic chains are very close each other and a little overlap of SOMO's on the phenylring is expected. This molecular arrangement between very close neighboring 4-nitrophenyl segments maybe results in the slight antiferromagnetic interaction .

3.3 Experimental Results and Discussion of NDV

3.3.1 Crystal Structure

3-Nitro-1,5-diphenylverdazyl (abbreviated as NDV) crystal was also prepared by Prof. Neugebauer's group. The crystal structure belongs to monoclinic ($P2_1/n$) with a = 3.9994 Å , b = 14.926 Å , c = 22.028 Å and β = 94.55 ° [45] as shown in Fig. 3.5.

The crystal structure of NDV obviously indicates that the verdazyl planes are stacked along a-axis giving a possibility of large SOMO-SOMO overlapping along this direction. It is also clear form Fig. 3.5.(c), that the verdazyl planes are separated away each other when viewed down from the a-axis. Therefore the intrachain interaction along the a-axis is supposed to be antiferromagnetic, and the interchain interactions are expected much weaker than the former.

3.3.2 Magnetic Susceptibility

The dc-magnetic susceptibility (χ_{dc}) was measured in the temperature region between 4.2 K and 100 K by a SQUID magnetometer (HOKUSAN HSM 2000). The diamagnetic contribution was calculated to be -0.139 $\times 10^{-3}$ emu/mol by the Pascal's law, and subtracted from the experimental value of χ_{dc}.

The results of χ_{dc} and χ_{dc}^{-1} are shown in Fig. 3.6. At higher temperatures than 20 K, χ_{dc} obeys the Curie-Weiss law (*eq*.3.1) with C = 0.350 emu·K/mol and Θ = -7.3 K, indicating the existence of the antiferromagnetic exchange interaction between neighboring radical molecules. Furthermore at lower temperature below 20 K, a broad peak characteristic of low-dimensional antiferromagnetic system is detected with its maximum around 7.0 K, as is speculated in subsection 3.3.1. So as the first approximation, χ_{dc} of NDV is analyzed as the S = 1/2 1D Heisenberg antiferromagnet (HAF), in which the maximum value (χ_{max}) and the corresponding temperature (T_{max}) are given as follows [36],

$$\frac{\chi_{max}}{g^2\mu_B^2/|J|} \simeq 0.07346 \quad , \tag{3.12}$$

$$\frac{k_B T_{max}}{|J|} \simeq 1.282 \quad . \tag{3.13}$$

The experimental results were reproduced by this model with T_{max} = 7.4 ± 0.2 K and J/k_B = -5.8 ± 0.2 K. This value of exchange interaction J/k_B gives the same order of the Weiss temperature observed above, which is theoretically expressed as

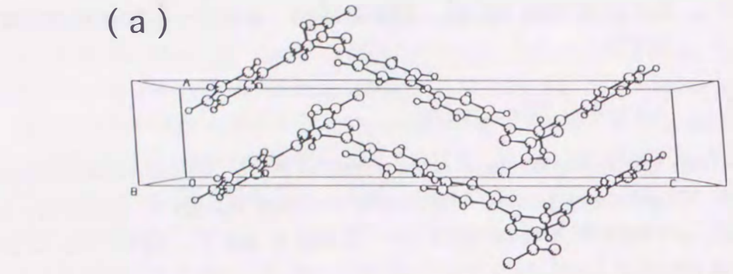

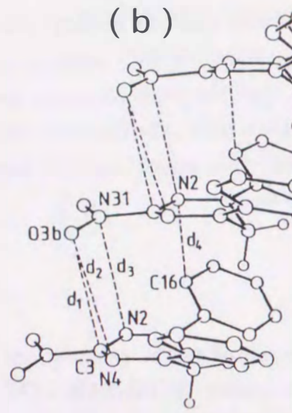

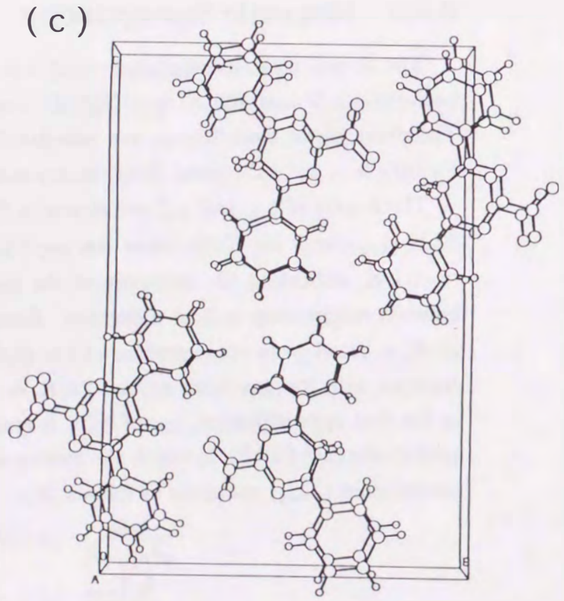

Figure 3.5: (a) Crystal stacking of NDV. (b) A side view showing the stair pattern and the intermolecular overlap between adjacent molecules. Shortest intermolecular distances within the stair pattern: d_1(O3b-C3^i)=3.44 Å , d_2(O3b-N4^i)=3.42 Å , d_3(N31-N2^i)=3.57 Å , d_4(N2-C16^i)=3.27 Å [symmetry code i; 1+x,y,z]. (c) View onto the verdazyl N1,N2,N4,N5 plane of NpTV showing from the direction of the chain.

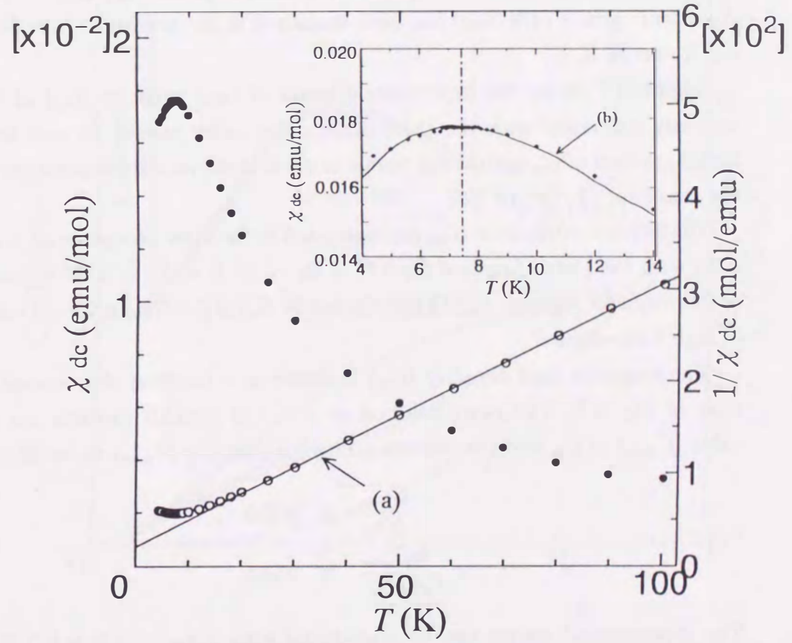

Figure 3.6: Temperature dependences of χ_{dc} and χ_{dc}^{-1} of NDV below 100 K. The straight line (a) expresses the Curie-Weiss (*eq*.3.1) law with $S = 1/2$ and Θ = -7.3 K. The solid curve (b) in the inset expresses the theory for 1DHAF [36] with J/k_B = -5.8 K and $S = 1/2$.

$$\Theta = \frac{2zJS(S+1)}{3k_{\rm B}} \quad , \tag{3.14}$$

where $z = 2$ is the number of the path of nearest neighboring interaction and $S = 1/2$.

3.3.3 Heat Capacity

The heat capacity of the polycrystalline sample (516.8 mg) of NDV mixed with Apiezon-N grease (478.5mg) has been measured in the temperature region between 0.8 K and 16 K.

Figure 3.7 shows the experimental result of heat capacity ($C_{\rm p}$) of NDV. The anomaly concerned with the three-dimensional order cannot be seen at all. The initial gradient of $C_{\rm p}$ against low temperature is linear on the temperature indicating the character of 1DHAF [36].

The lattice contribution ($C_{\rm l}$) was estimated in the same procedure as in subsection 3.2.3 with the Debye function (*eq*.3.7) of $\Theta_{\rm D} = 97$ K and $r = 3$, in which the value of the magnetic entropy $S_{\rm m}(T)$ approaches to $S_{\rm m}(\infty) = Nk_{\rm B}ln(2S+1)$ at the limit of high temperature.

The magnetic heat capacity ($C_{\rm m}$) is shown as a function of temperature in the inset of Fig. 3.7. The exact solution of $S = 1/2$ 1DHAF predicts the maximum value ($C_{\rm max}$) of $C_{\rm m}$ and the corresponding temperature ($T_{\rm max}$) to be [36],

$$\frac{C_{\rm max}}{Nk_{\rm B}} \simeq 0.350 \quad , \tag{3.15}$$

$$\frac{k_{\rm B}T_{\rm max}}{|J|} \simeq 0.962 \quad . \tag{3.16}$$

The experimental results can be reproduced with $J/k_{\rm B}$ = -5.3 $\pm$ 0.2 K, giving a reasonable value for that obtained in the analysis of $\chi_{\rm dc}$.

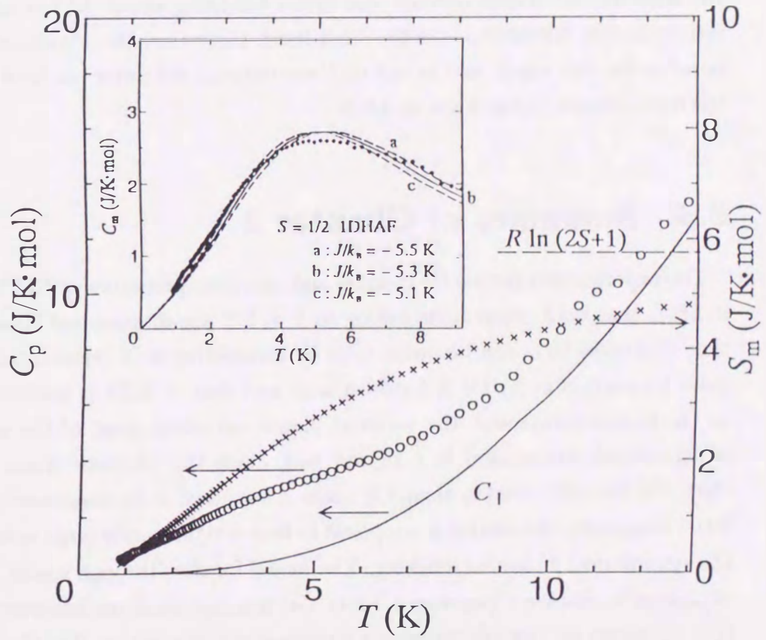

Figure 3.7: Temperature dependences of heat capacity ($C_{\rm p}$; o) of NDV and magnetic entropy ($S_{\rm m}$; ×) below 16 K. The solid curve expresses the lattice contribution ($C_{\rm l}$) which is the Debye function (*eq*.3.7) with $\Theta_{\rm D} = 97$ K and $r = 3$. The inset demonstrates the temperature dependence of magnetic heat capacity ($C_{\rm m}$; •) below 9 K, together with three solid and broken curves (a-c) of the theory of $S = 1/2$ 1DHAF [36].

3.3.4 Conclusion of NDV

The experimental results of χ_{dc} and C_m indicate that NDV is magnetically approximated as a good one-dimensional Heisenberg system (uniform chain) with the antiferromagnetic intrachain interaction of J/k_B = -5.5 ± 0.5 K.

The direction of linear chain is supposed to be a-axis from the consideration of the crystal structure. The symmetrical molecular stacking along the a-axis suggests the large SOMO-SOMO overlap, and hence will bring about the antiferromagnetic intermolecular interaction. On the other hand, the interchain orbital overlap is supposed to be very small, and in fact no three-dimensional order has been detected in the temperature region down to 0.8 K.

3.4 Summary of Chapter 3

The experimental results for thermal and magnetic properties of NpTV and NDV indicate that both compounds belong to $S = 1/2$ one-dimensional Heisenberg system, and these facts can be understood by considering each crystal structure. The main interaction in NpTV is ferromagnetic and that of NDV is antiferromagnetic. In the former compound, the verdazyl planes, on which most of the spin density is delocalized, are stacked in a zig-zag path along the magnetic chain. Therefore the SOMO-SOMO overlap along the chain is supposed to be suppressed, but in the latter compound the overlap is supposed to have a significantly large value reflecting the symmetrical molecular stacking. The model for the "through space" interaction explained in chapter 1 (sections 1.3 and 1.4) has suggested the following condition: It is necessary for the intermolecular ferromagnetic interaction that the component molecules are stacked with the orthogonal SOMO's overlapping in the crystallized state. The molecular stacking of NpTV satisfies this condition, and that of NDV does not. The experimental results of NpTV and NDV in chapter 3 indicate that the reduction of the SOMO-SOMO overlap becomes very important factor to bring about the ferromagnetic parallel spin alignment by the "through space" interaction.

Chapter 4

Two-Dimensional Heisenberg Antiferromagnet with Weak-Ferromagnetic Moment: 1,3,5-Triphenyl-6-Oxoverdazyl

4.1 Introduction

We have already mentioned that the organic magnets provide the ideal Heisenberg system with quite a small anisotropy. There are many theoretical studies of the quantum statistics in low-dimensional (1D and 2D) Heisenberg systems. As for the organic one-dimensional (1D) system, there are many experimental reports which testify the interest of the quantum statistical theories [6,15,16,17,20,49] without stepping into the mechanism of one-dimensional magnetic interactions from the stand point of materials science. The experimental results of ferromagnetic γ-phase *p*-NPNN [6,49], *p*-CDTV [15,16] and *p*-CDpOV [17] have typically shown the characteristic quantum properties of the 1D Heisenberg ferromagnetic system.

For the organic two-dimensional (2D) Heisenberg system, however, there has not been the experimental study concerned to the quantum statistics yet. The discovery of the high T_c superconductors of La_2CuO_4 family compounds [50] has urged the development of the study of the two-dimensional (2D) quantum Heisenberg antiferromagnet (HAF) with the spin $S = 1/2$. The ground state properties [51-53] and finite-temperature properties such as the spin correlation length [53-58], have been theoretically investigated by a variety of methods. The corresponding experimental studies of the correlation length for 2DHAF, however, are limited to the paramagnetic region of the La_2CuO_4 series with the high ordering temperature

($T_N \sim 300$ K) [59,60].

This chapter reports the experimental data of thermodynamic quantities of a 2D organic radical crystal 1,3,5-triphenyl-6-oxoverdazyl (**TOV**) to be analyzed quantitatively with the quantum statistical theories for the 2D system. Secondly this chapter mentions about the weak-ferromagnetism in TOV, from which the staggered susceptibility for the 2D Heisenberg system with $S = 1/2$ will be derived, and the spin dimensional crossover from 2D Heisenberg to 2D Ising systems will be suggested in the reference of the scaling relation between spin correlation length and magnetic susceptibility for the 2D quantum system.

Finally we mention about the origin of weak-ferromagnetism of this compound from the stand point of materials science. Weak-ferromagnetism has rarely been studied in genuine organic systems, and its mechanism in radical substances has not been cleared. Generally a weak-ferromagnetic moment is relevant to such anisotropy as the antisymmetrical exchange interaction or the single ion anisotropy. We will represent that the weak-ferromagnetism of TOV originates from the Dzyaloshinsky-Moriya (D-M) interaction [61], which belongs to the antisymmetrical exchange interaction. We also suggest that there exists a limit for enlarging spontaneous magnetization in organic molecule-based magnets.

4.2 Previous Results

The crystal structure of TOV at room temperatures (Fig. 4.1) has already been reported together with the result of electron paramagnetic resonance (EPR) [62]. Figure 4.1(a) and Fig.4.1(b) respectively show the molecular structure and the molecular stacking projected down on the *bc*-plane. The McLachlan molecular orbital calculation gives the distribution of the spin density as seen in Fig. 4.2 [44], and suggests the π-SOMO is mainly confined on four nitrogens of the central verdazyl ring. The crystal structure of TOV belongs to the space group $C_{2/c}$ with $a = 19.213$ Å , $b = 11.392$ Å , $c = 7.304$ Å and $\beta = 90.72$ °. The nearly planar structure of TOV molecule has a twofold symmetry axis going through C(4"), C(1"), C(3), C(6) and O as shown in Fig.4.1(a). There exists the inversion center between adjacent two molecules respectively on A- and B- sublattices as shown in Fig.4.1(b). Fig.4.1(c) and Fig.4.1(d) show the crystal structures projected on the *ac*-plane and the *ab*-plane, respectively. The overlapping of molecular orbitals of π-electrons along the *b*-axis is expected much weaker than that on the *ac*-plane. The EPR measurement

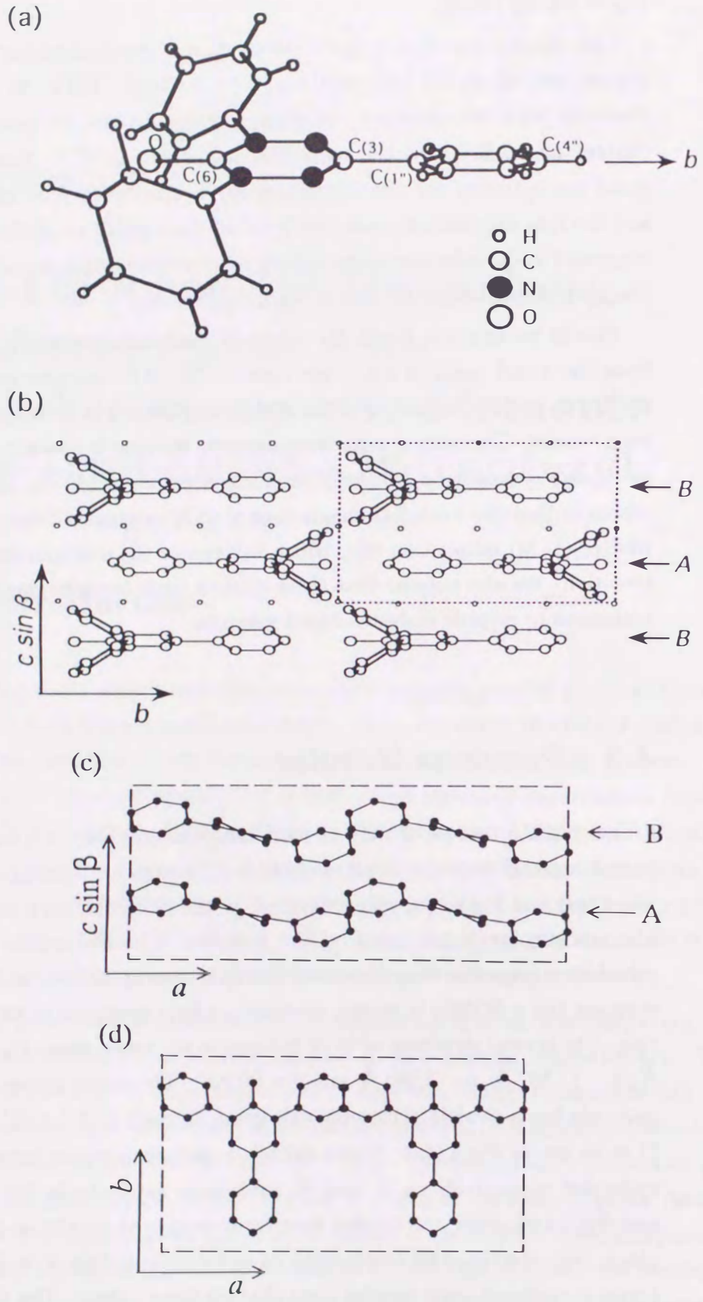

Figure 4.1: Molecular structure (a) of TOV and molecular stackings projected down on the *bc*-plane (b), the *ac*-plane (c) and the *ab*-plane (d). The division line expresses the unit cell.

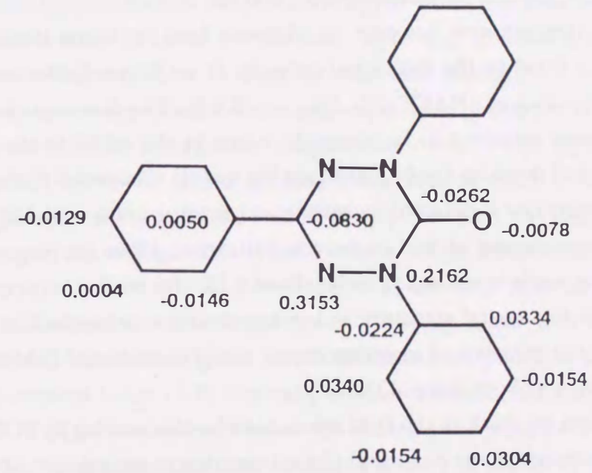

Figure 4.2: Spin density distribution of TOV by the McLachlan molecular orbital calculation [44]. The spin density on four nitrogens of the central verdazyl ring is extremely high.

at room temperatures has shown that TOV has an isotropic g-value $g_{iso} = 2.0037$.

The single ion anisotropy is not expected in the organic radical system with $S = 1/2$, and the magnetic dipolar interaction between the nearest neighbor radicals in TOV is very small, as estimated to be 125 Gauss from the spin density based on the McLachlan calculation mentioned above.

The magnetic properties and microwave properties have been already studied [63]. The static magnetic susceptibility (χ_{dc}) above 100 K obeys the Curie-Weiss law with the negative Weiss temperature Θ = -12 $\pm$ 2 K with nearly an ideal value of Curie constant C = 0.38 $\pm$ 0.01 K $\cdot$ emu / mol for $S = 1/2$ and $g = 2.00$. These results indicate that the dominant exchange interaction between unpaired electrons of adjacent verdazyls is antiferromagnetic, and one spin of $S = 1/2$ exists per molecule. At lower temperatures, however, χ_{dc} deviates from the Curie-Weiss law and χ_{dc} above 15 K is fitted by the theoretical curve for $S = 1/2$ one-dimensional (1D) Heisenberg antiferromagnet (HAF) with J/k_B = - 8.6 K. The direction of the magnetic chain had been supposed to be along the c-axis in the ref.62 to the molecular stacking projected down on the bc-plane (see Fig.4.1(b)). Below 4.9 K the weak spontaneous magnetization is detected increasing and turning to decrease slightly below 2.0 K in the measurement of field cooled magnetization. From the magnetization at 2.0 K a canting angle is estimated to be about 0.13 ° for the saturation moment with $S = 1/2$. If the crystal structure at low temperature maintains that at room temperatures, the presence of inversion center would exclude the D-M interaction between two spins at both sides of the center.

When we stuck to the D-M interaction for this canting in TOV, we first expected the existence of the structural phase transition at intermediate temperatures, which lower the crystallographic symmetry to bring about the D-M interaction along the c-axis. But in the measurement of differential scanning calorimetry above *liq*.N_2 temperature, any anomaly which indicates the structural phase transition could not be detected. In this chapter we make the weak ferromagnetism of TOV at the ambient pressure clear experimentally, and discusses the possibility and/or validity of the D-M interaction. At the last part of this chapter (especially in subsection 4.3.6), we propose a model from which the weak-ferromagnetic moment is deduced in TOV.

4.3 Experimental Results and Discussion

The radical crystal of TOV was synthesized according to the procedure indicated in ref.62 by Prof. Mukai's group (Ehime University). The shape of the TOV crystal, which was used in following experiments, was slender like needle along the c-axis.

4.3.1 Heat Capacity

The heat capacity was measured by an adiabatic method in the temperature region from 0.6 K to 30 K. The Apiezon-N grease (0.4483 g) for thermal binder was mixed with the polycrystalline sample (0.3407 g) of TOV. The heat capacity of the addenda (thermometer, heater, Cu platform, Apieson-N grease etc.) amounts to about 5 % at 5 K and 76 % at 15 K for the total heat capacity.

The temperature dependence of the heat capacity (C_p) of TOV is shown in the logarithmic scale in the temperature range between 0.63 K and 30 K in Fig. 4.3. The broken line in Fig. 4.3 shows the lattice contribution which is estimated with the Debye function $f(\Theta_D = 95$ K, $r = 3)$ of *eq*.3.7, so that the magnetic entropy $S(T)$ becomes $S(\infty) = Nk_B ln(2S+1)$ at the limit of high temperature. The lattice contribution is 18.6 % at 5.0 K, 72.8 % at 10 K and 97.5 % at 20 K. Then the experimental ambiguity of the magnetic heat capacity below 5 K is not serious for the following discussion. Figure 4.4 shows that about 86.0 % of total magnetic entropy is consumed below 15 K. Generally in three-dimensional Heisenberg system, about 60 % of $S(\infty)$ is consumed below the ordering-temperature T_c [64]. In the case of TOV, the residual magnetic entropy below T_c is about 45 %, where the value of T_c is estimated as T_c = 4.8 K (as will be referred to in subsection 4.3.6). This indicates that the magnetic properties of TOV shows the feature of the low-dimensional magnetic system. After all the measurements of heat capacity in the temperature region below 30 K do not indicate any anomaly, which concerns a structural phase transition lowering the crystallographic symmetry to yield the D-M interaction mentioned in section 4.2.

Figure 4.5 shows the magnetic heat capacity (C_m) below 12 K. The magnetic heat capacity is gotten by subtracting the lattice contribution from C_p. The data of C_m above 8.0 K have some ambiguity, because contributions from the addenda and the lattice become relatively larger than C_m. The remarkable point is the existence of broad maximum associated with the short range ordering effect. In the previous analysis of magnetic susceptibility by Kremer *et al.* [63], the magnetic system of TOV has been considered to be one-dimensional. Our results of C_m, however, cannot

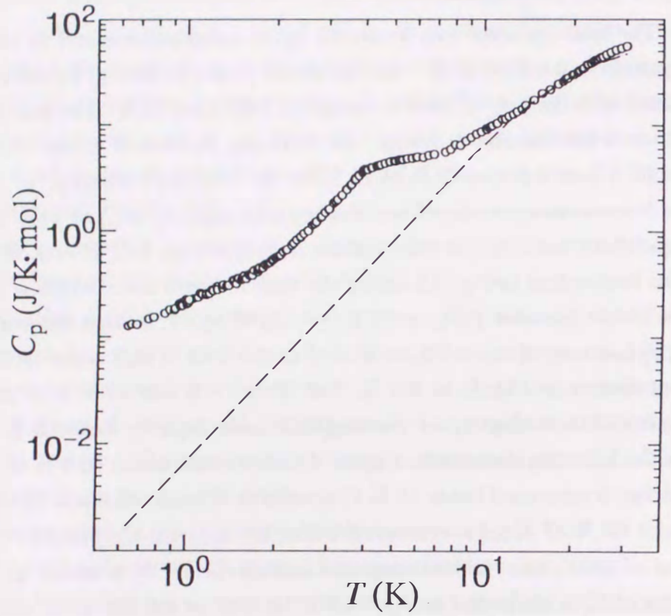

Figure 4.3: Temperature dependence of heat capacity C_p of TOV in the logarithmic scale. The broken line shows the lattice contribution which is estimated with the Debye function (*eq*.3.7) with $\Theta_D = 95$ K and $\boldsymbol{r} = 3$.

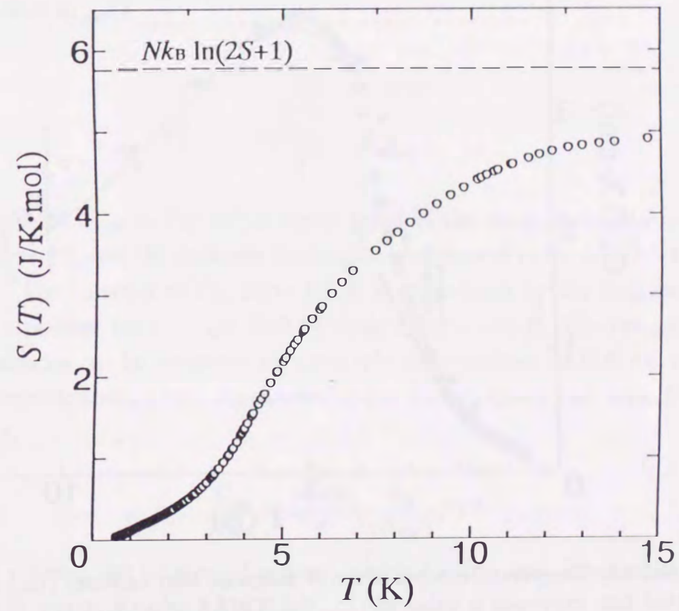

Figure 4.4: Temperature dependence of magnetic entropy (S) of TOV. The broken line shows the total magnetic entropy $S(\infty) = Nk_B ln(2S + 1)$ for S =1/2.

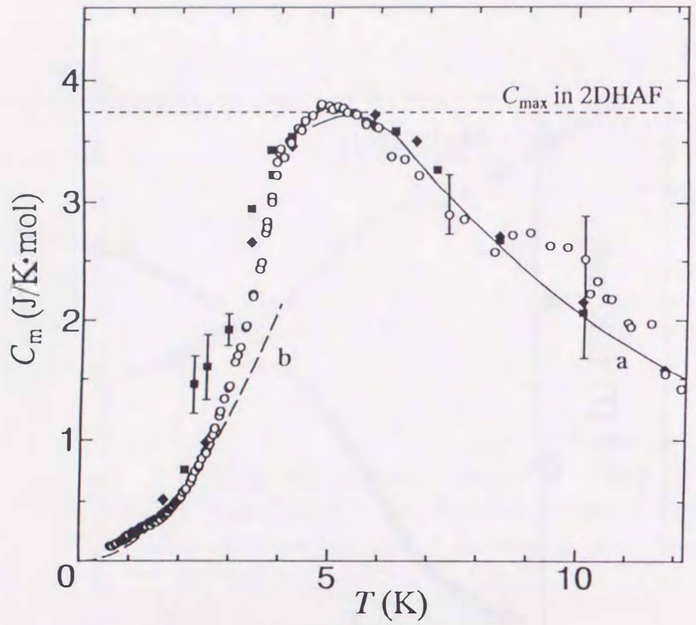

Figure 4.5: Temperature dependence of magnetic heat capacity (C_m) of TOV. The dotted line expresses a value of C_{max} in 2DHAF with $S = 1/2$. (a): The high temperature series expansion for $S = 1/2$ 2DHAF [65] with J/k_B = -4.2 K, (b): Takahashi's spin wave theory for $S = 1/2$ 2DHAF [67] with J/k_B = -3.7 ± 0.1 K or Kubo's one [66] with J/k_B = -4.3 ± 0.1 K, (◆, ■): the Monte Carlo simulations for $S = 1/2$ 2DHAF with J/k_B = -4.2 K by Okabe *et al.* [53] and Makivić *et al.* [57], respectively.

be reproduced with the theory for $S = 1/2$ 1DHAF, which gives linear temperature dependence at low temperatures and the maximum value of $C_m = 0.35\ Nk_B$ (2.9 J/K · mol). According to the high temperature series expansion for 2DHAF with $S = 1/2$ [65] where the Hamiltonian of the system is expressed as

$$\mathcal{H} = -\sum_{i,j} 2JS_i \cdot S_j \quad , \tag{4.1}$$

the maximum value (C_{max}) of C_m and the corresponding temperature (T_{max}) with C_{max} are respectively given as follows:

$$\frac{C_{max}}{Nk_B} \sim 0.45 \quad , \tag{4.2}$$

$$\frac{k_B T_{max}}{|J|} \sim 1.3 \quad . \tag{4.3}$$

Our value of C_{max} in Fig. 4.5 is nearly equal to the value (0.45 $Nk_B \simeq$3.7 J/K · mol) of *eq.*4.2, and the exchange interaction is estimated to be $J/k_B \simeq$ -4.2 K from *eq.*4.3. The behavior of C_m above 5.0 K is reproduced by the high temperature series expansion for $S = 1/2$ 2DHAF with J/k_B = -4.2 K. The low-temperature heat capacity can be compared with two spin wave theories for 2DHAF, which give the quadratic temperature dependence of C_m; Kubo's theory [66] with J/k_B = -4.3 ± 0.1 K

$$\frac{C_m}{Nk_B} = \frac{14.424}{\pi}\left(\frac{k_B}{2z|J|S}\right)^2 T^2 \quad , \tag{4.4}$$

where z being the number of nearest neighbor spins, and Takahashi's quantum theory [67] with J/k_B = -3.7 ± 0.1 K,

$$\frac{C_m}{Nk_B} = \frac{3\zeta(3)k_B^2}{4\pi(2|J|m)^2} T^2 \quad , \tag{4.5}$$

where $\zeta(3)$ being the Riemann function and $m = S + 0.078974$.

In wider temperature region, the data of C_m are well reproduced by two quantum Monte Carlo simulations [53,57] for $S = 1/2$ 2DHAF with J/k_B = -4.2 K. After all, the behavior of C_m in Fig. 4.5 is explained for $S = 1/2$ 2DHAF with $J/k_B \simeq$ -4.2 K. We think that the 2D antiferromagnetic plane will spread along the *ac*-plane, because the overlapping of molecular orbitals of π-electrons along *b*-axis can be hardly expected as seen in Fig.4.1. The intermolecular exchange interaction, of course, may be not identical along the *a*- and *c*-axes, and the value of J/k_B estimated

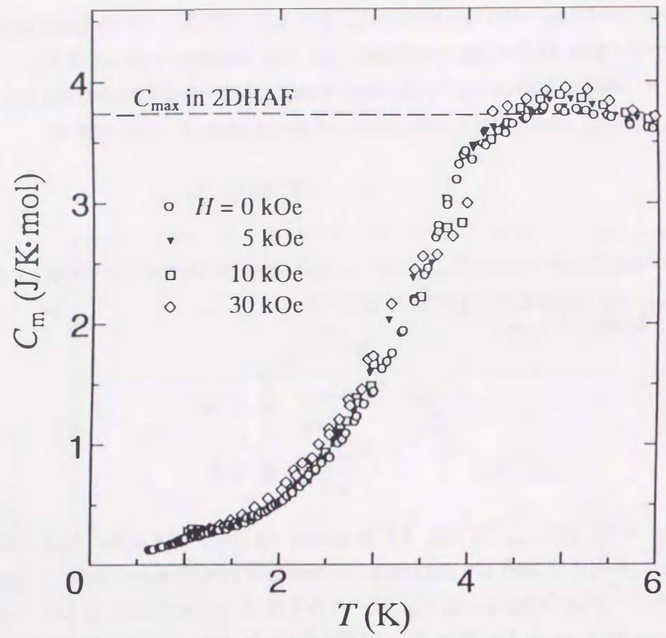

Figure 4.6: Magnetic heat capacity of TOV below 6.0 K in the external fields; H = 0 kOe(○), 5 kOe(▼), 10 kOe(□) and 30 kOe(◇).

here is an effective or averaged one. The strong quantum effect of the isotropic spin with $S = 1/2$ may positively act in this averaging.

Figure 4.6 shows the temperature dependence of C_m in the external field (H) up to 30 kOe, in order to confirm that the peak of C_m around 5.0 K depends on the antiferromagnetic short range order.

Even in H = 30 kOe, the behavior of C_m below 6.0 K changes little. This insensitivity to magnetic fields is reasonable for the antiferromagnetic feature of this system. In the molecular field theory, the exchange field (H_{ex}) is expressed as follows:

$$H_{ex} = \frac{2z|J|\langle S\rangle}{g\mu_B} \quad , \tag{4.6}$$

where g and μ_B respectively express the g-value and the Bohr magneton. Numerical calculation for z = 4 and J/k_B = -4.2 K yields H_{ex} = 125 kOe. The strength of H = 30 kOe is about 24 % of the exchange field H_{ex}, giving little effect to break the singlet spin pairings in the case of ordinary antiferromagnets.

It has been rigorously proved that the spontaneous magnetization does not ap-

pear at a finite temperature in the ideal 2D Heisenberg system *. Any evidence of long range ordering cannot be seen in the results of heat capacity of TOV as shown in the present work. As will be revealed in the next subsection, however, the magnetic susceptibility does exhibits an abrupt increase just below 6 K, which cannot be expected for the isotropic 2D Heisenberg system. There we also mention about the possibility of the magnetic ordering in the 2D quantum lattice.

4.3.2 Zero-Field Magnetic Susceptibility

The *ac*-magnetic susceptibility (χ_{ac}) for the polycrystalline TOV (31.6mg) in zero external field was measured with the Lakeshore 7110 AC Susceptometer which operated for the *ac*-field (H_{ac}) up to 10 Oe (peak-to-peak) at the frequencies (f) of 5, 48, 125, 500, 1000 Hz and the temperature region from 2.1 K to 150 K. The observation of χ_{ac} in the temperature region from 0.7 K to 10 K was performed by another Hartshorn bridge method (H_{ac} = 0.6 Oe (peak-to-peak) and f = 100 Hz) simultaneously with the measurement of heat capacity.

Figure 4.7 shows the real part (χ_{ac}) of the *ac*-magnetic susceptibility and the inverse susceptibility (χ_{ac}^{-1}) in the temperature region from 2.1 K to 80 K for the *ac*-field of f = 125 Hz.

The intrinsic χ_{ac} of TOV is obtained by subtracting a very small diamagnetic contribution (-0.221 × 10^{-3} emu / mol), which is 1.5 % at 10 K and 14.5 % at 150 K to the total χ_{ac}. The rapid increasing of χ_{ac} can be seen below 6.0 K. On the other hand, the inverse susceptibility above 20 K obeys the Curie-Weiss law (*eq*.3.1) with the negative Weiss temperature (Θ = -9.9 K), and the ideal Curie constant (C = 0.375 emu · K / mol) for $S = 1/2$ and g = 2.00. This indicates that an antiferromagnetic interaction is dominant and an unpaired electron exists per a molecule. This negative Weiss temperature and the rapid increasing of χ_{ac} below 6.0 K indicate that TOV is weak-ferromagnetic. Above results are consistent with the results in ref.63. Any significant frequency dependence of χ_{ac} could not be seen in the frequency region from 5 Hz to 1 kHz.

In Fig. 4.8, we analyze the temperature dependence of χ_{ac} below 40 K, with following three theories; (1) the Curie-Weiss law, (2) the high temperature series expansion for $S = 1/2$ 2DHAF [65], and (3) the Monte Carlo simulations for $S = 1/2$ 2DHAF [53,57]. The results of χ_{ac} below 20 K deviate from the Curie-Weiss law mentioned above, where the magnetic short range ordering starts gradually. In

*by N.D.Mermin and H.Wagner: Phys.Rev.Lett.17(1966)1133.

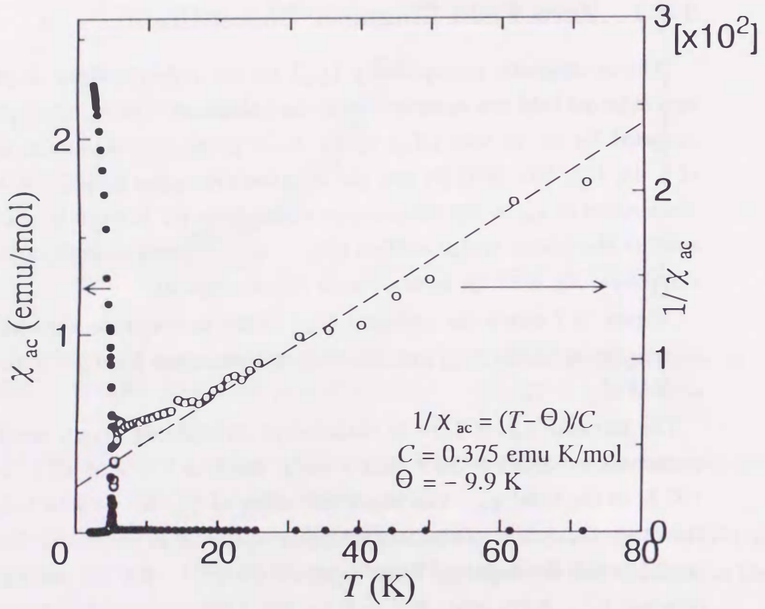

Figure 4.7: Magnetic susceptibility (•) and the inverse susceptibility (○) of TOV in zero external field. The broken line shows the Curie-Weiss law with Θ = -9.9 K and C = 0.375 emu · K / mol.

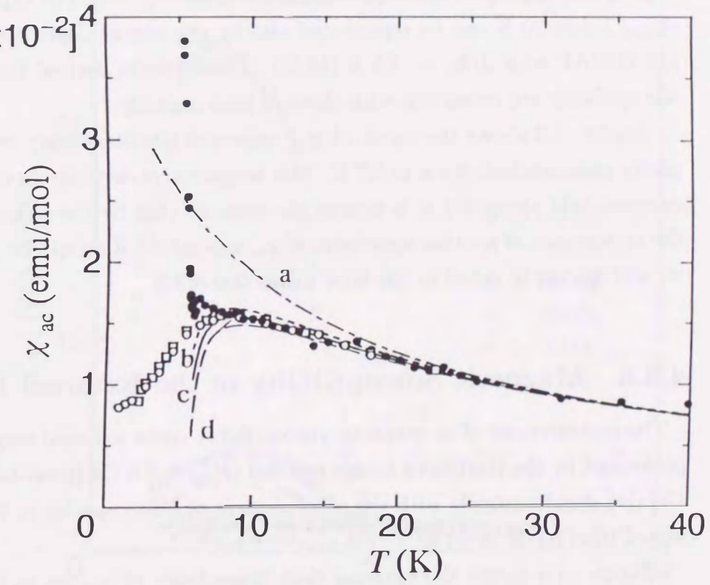

Figure 4.8: Magnetic susceptibility (•) of TOV below 40 K. (a): The Curie-Weiss law with Θ = -9.9 K and C = 0.375 emu · K / mol, (b ∼ d): the high temperature series expansion of S = 1/2 2DHAF [65] with J/k_B = -4.3 K (b), -4.5 K (c), -4.7 K (d) respectively, (○, □): the Monte Carlo simulations of S = 1/2 2DHF with J/k_B = -4.5 K by Okabe *et al.* [53] and Makivić *et al.* [57], respectively.

the molecular field theory, the Weiss temperature (Θ) is given as *eq*.3.14. Putting the observed value of Θ = -9.9 K assuming $z = 4$, the value of J/k_B is estimated to be -4.5 K. The results of χ_{ac} above 8.0 K has a reasonable agreement with the high temperature series expansion of $S = 1/2$ 2DHAF for J/k_B = -4.5 K $\pm$ 0.2 K, where χ has its maximum at the following temperature [65]

$$T_{max} \simeq (1.89 \pm 0.04)\ \frac{|J|}{k_B} \quad , \tag{4.7}$$

even in the vicinity of the broad maximum as in Fig. 4.8. The experimental result of χ_{ac} below 20 K can be reproduced also by the Monte Carlo simulations of $S = 1/2$ 2DHAF with $J/k_B \simeq$ -4.5 K [53,57]. These results derived from the magnetic susceptibility are consistent with those of heat capacity.

Figure 4.9 shows the result of χ_{ac} measured simultaneously with the heat capacity measurement down to 0.7 K. This temperature dependence of χ_{ac} under zero external field above 2.0 K is almost the same as that by the susceptometer. Here the appearance of another maximum of χ_{ac} around 2.0 K should be noted, on which we will discuss in detail in the later subsection 4.3.6.

4.3.3 Magnetic Susceptibility in the External Field

The measurement of *ac*-magnetic susceptibility under external magnetic fields was performed by the Hartshorn bridge method (H_{aca} = 0.6 Oe (peak-to-peak) and f = 100 Hz) simultaneously with the measurement of heat capacity in the temperature region from 0.7 K to 10 K.

Figure 4.9 shows the external field dependence of χ_{ac} up to 3 kOe, and the remarkable magnetic field dependence of χ_{ac} is observed. Even small external field such as 50 Oe is enough to suppress the broad maximum down to about one sixth of its height at zero field. The external magnetic field of 1 kOe makes the ferromagnetic moment quenched. When J/k_B = -4.5 K, which is estimated in Fig. 4.8, is adopted, the broad maximum of the susceptibility for $S = 1/2$ 2DHAF is expected to appear at $T_{max} \simeq$ 8.5 K from *eq*.4.7. The broad maximum is seen in the result for H = 3 kOe.

Taking these results into consideration, we may assume the following Hamiltonian

$$\mathcal{H} = -\sum_{i,j}\{2JS_i \cdot S_j + D_{i,j} \cdot (S_i \times S_j)\} + \sum_i g\mu_B S_i H \quad . \tag{4.8}$$

The above experimental results that the weak ferromagnetic moment disappears even in H = 1 kOe implies that the second and third terms in *eq*.4.8 effectively

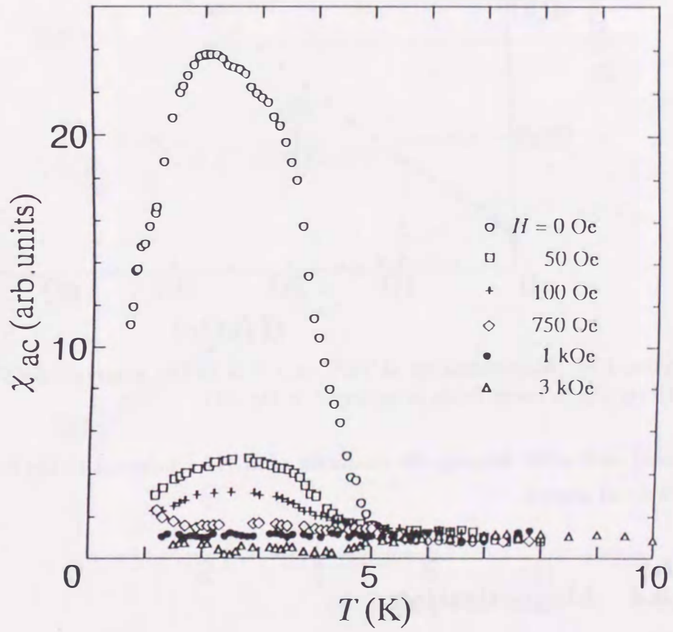

Figure 4.9: Magnetic susceptibility of TOV under the external field up to 3 kOe. The external fields are H = 0 Oe (○), 50 Oe (□), 100 Oe (+), 750 Oe (◇), 1 kOe (•) and 3 kOe (△).

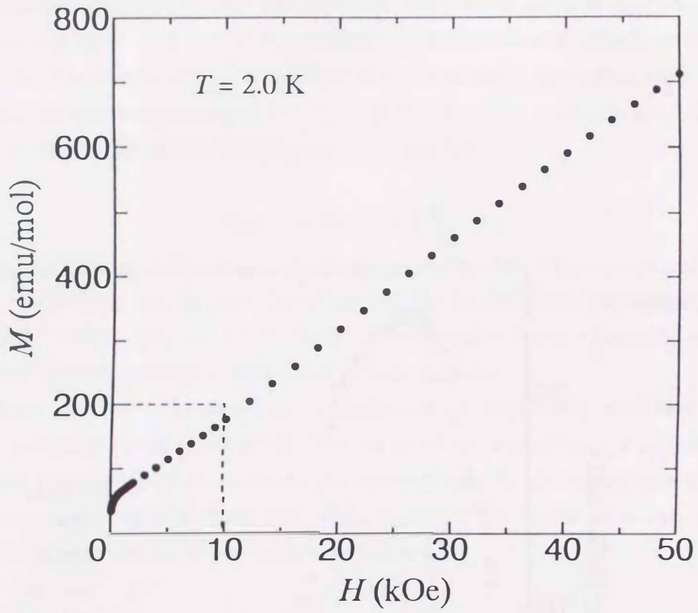

Figure 4.10: Magnetization of TOV at 2.0 K in the magnetic field up to 50 kOe. The results in lower fields is enlarged in Fig.4.11.

cancel each other keeping the character of 2DHAF inherent to the first term in this powdered sample.

4.3.4 Magnetization

The magnetization of the polycrystalline TOV (56.7 mg) was measured with the SQUID magnetometer at 2.0 K and 3.0 K up to the external field of 50 kOe. The magnetization at 2.0 K is shown in Fig. 4.10. In Fig. 4.11, the magnetization at 2.0 K and 3.0 K below 10 kOe is given in detail.

In low magnetic fields, the magnetization M is expressed as follows:

$$M = M_0 + \chi H \quad , \tag{4.9}$$

where M_0 is a spontaneous magnetization at $H = 0$. The value of M_0 is estimated to be 53.5 emu/mol at 2.0 K and 51.8 emu/mol at 3.0 K. At 2.0 K, which is less than half of $T_c = 4.8$ K, the canting angle ϕ is estimated to be 0.27° from $M_0 = 2M_s \sin\phi$, where M_s is the saturation moment ($M_s = Ng\mu_B S$) for $S = 1/2$ and ϕ is the angle

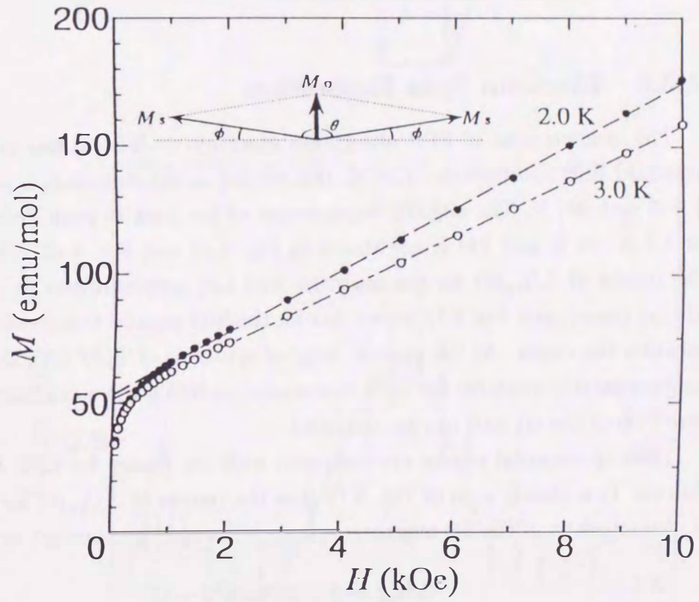

Figure 4.11: Magnetization of TOV at 2.0 K (•) and 3.0 K (○) below 10 kOe. M_0 is a spontaneous magnetization at $H = 0$, and M_s is the saturation moment ($M_s = Ng\mu_B S$).

indicated in Fig. 4.11 ($\theta = \pi - 2\phi$). The value of D is evaluated from the condition $\partial\langle\mathcal{H}\rangle/\partial\theta = 0$, which yields the following relation

$$\tan(\theta) = |\frac{D}{2J}| \quad . \tag{4.10}$$

At 2.0 K, the value of $|D/2J|$ is estimated to be 9.6 $\times$ 10^{-3} from *eq.*4.10, and hence D/k_B is estimated to be 8.6 $\times$ 10^{-2} K in the case of J/k_B = -4.5 K. This value of D/k_B corresponds to 1.3 kOe, which is nearly equal to the value of the magnetic field which makes the susceptibility quenched as discussed in subsection 4.3.3.

4.3.5 Electron Spin Resonance

The measurement of EPR absorption spectrum at X-band was performed by a standard ESR spectrometer (JEOL JES-RE2X) in the temperature region between 1.4 K and 290 K. The angular dependences of the peak-to-peak linewidth (ΔH_{pp}) at 4.2 K, 89 K and 290 K are shown in Fig. 4.12 and Fig. 4.13. Fig. 4.12 shows the results of $\Delta H_{pp}(\theta)$ for the magnetic field (H) perpendicular to the c-axis (i.e. $H//ab$-plane), and Fig. 4.13 shows that for the field parallel to a certain plane which includes the c-axis. At the present stage of synthesis of TOV crystal, only a small single crystal is available for EPR experiment, in which the c-axis (along the needle direction of the crystal) can be identified.

The experimental results are compared with the theory for EPR on 2DHAF as follows. It is clearly seen in Fig. 4.12 that the results of $\Delta H_{pp}(\theta)$ for $H//ab$-plane is characteristic of the 2D magnetic system [68] which is expressed as

$$\Delta H_{pp} = A + B(3\cos^2\theta - 1)^2, \tag{4.11}$$

where the angle θ corresponds to the field direction measured from the perpendicular axis to a 2D plane. This theory gives a maximum linewidth at $\theta = 0°$, where the field is along the perpendicular axis. With the values of A = 0.22 and B = 0.105 Oe, a satisfactory fit for the 2D magnetic system is obtained. From the crystal structure of TOV, it is noticed that the overlapping of molecular orbitals of π-electrons along the b-axis is expected much weaker than that on ac-plane, as seen in Fig. 4.1. Here we regard that the 2D magnetic ordering plane is the ac-plane. Figure 4.13 shows the results of $\Delta H_{pp}(\theta)$ for the magnetic field parallel to a certain plane which includes the c-axis. We could not observe the angular dependence of ΔH_{pp} peculiar to the 2D system as detected in Fig. 4.12, because the a-axis or b-axis might not exist on the plane containing the direction of the magnetic field. It is commented here that the

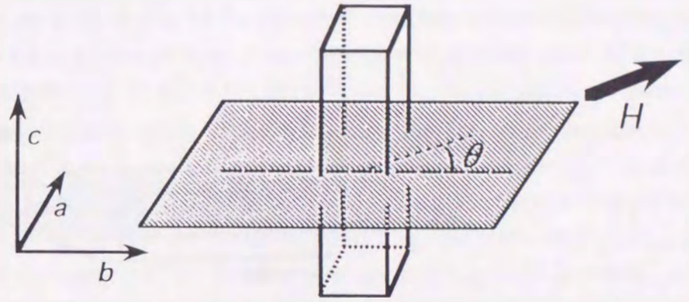

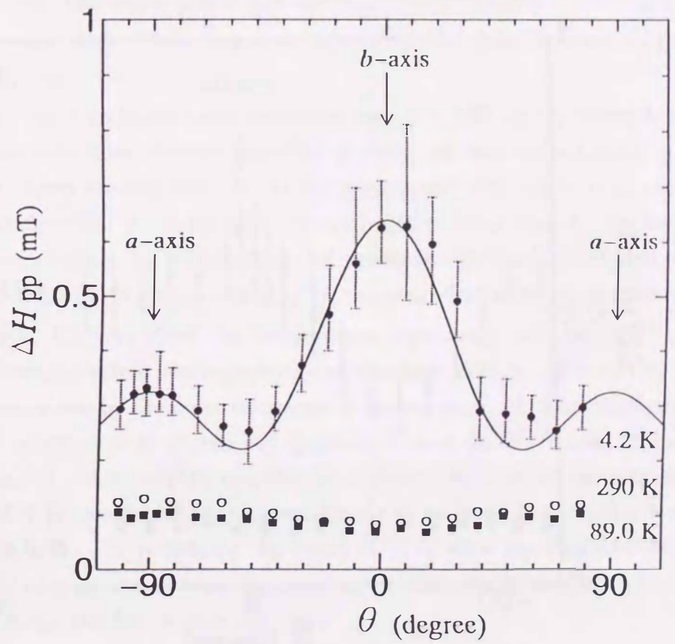

Figure 4.12: The EPR experimental results for the angular dependences of the peak-to-peak linewidth (ΔH_{pp}) of TOV for $H \perp c$-axis (i.e. $H//ab$-plane) at 4.2 K (•), 89.0 K (■) and 290 K (○). θ corresponds to the field direction measured from the perpendicular axis for the 2D plane.

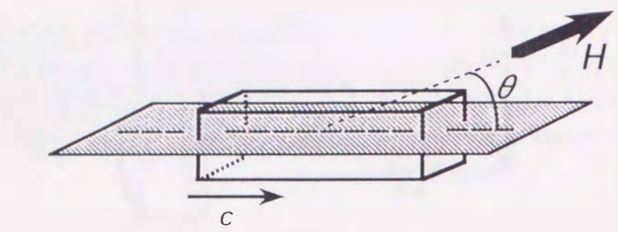

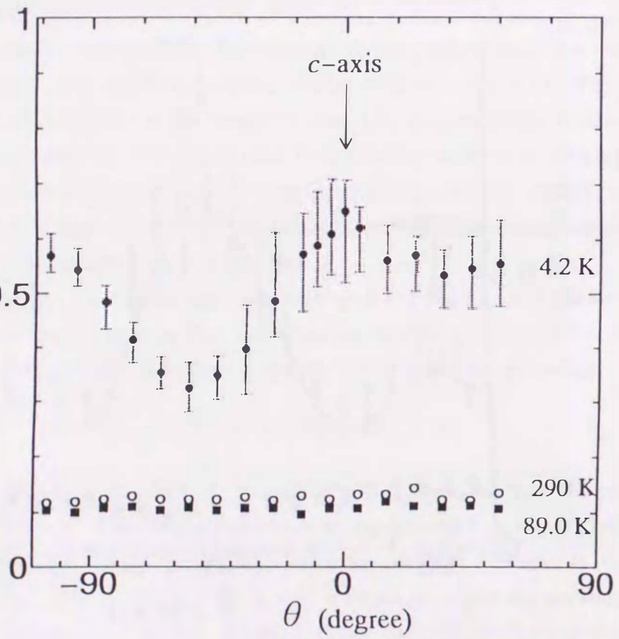

Figure 4.13: The EPR experimental results for the angular dependences of the peak-to-peak linewidth (ΔH_{pp}) of TOV for $H//$a certain plane including the c-axis.

resemble angular dependence of ΔH_{pp} should be observed in the results at 89 K and 290 K, if the 2D magnetic structure in TOV is maintained at higher temperature. The reasons, we think of, may be the change of temperature dependence of magnetic interactions via molecular orbitals or the experimental error for small EPR signals at higher temperatures, in which the intrinsic angular dependence might exist.

In the spin diffusion model of the 2D system, the Lorentzian lineshape of the integral intensity $I(H)$ is expected at the magic angle $\theta_m = 54\,^\circ$, but $I(H)$ for $\theta \neq \theta_m$ deviates from this [68], where θ is taken as in Fig. 4.12. For the examination of the lineshape of TOV, we plot the quantity $[I(H)]^{-1}$ against $[(H - H_0)/(\Delta H_{1/2}/2)]^2$, where H_0 is the resonance field and $\Delta H_{1/2}$ is the half-amplitude linewidth. For a Lorentzian, this plot gives a straight line in above scale. Figure 4.14 shows the experimental results at 4.2 K for $\theta = -2°$ (nearly $H//b$-axis), -52° and -92°(nearly $H//a$-axis). The nearly Lorentzian lineshape is observed at θ = -52° which is nearest to the magic angle. These results are consistent with those reported for the 2DHAF K_2MnF_4 [68].

Next Fig. 4.15 shows some derivative lines (dI/dH) for $H//b$-axis below 8.1 K. The derivative lines observed above 8.1 K, although they are not given in Fig. 4.15, are very sharp like that at 8.1 K. As the temperature approaches to T_c, the lineshape becomes broader. When the temperature becomes lower than T_c, the lineshape become more broader by the influence of the magnetic short range ordering of 2DHAF, but the condition of resonances H_0/f (f; resonance frequency) do not change largely.

In Fig. 4.16, we show the temperature dependence of g-values for each axis. Before these g-values are estimated, the magnetic field is calibrated by the NMR tesla meter and by the quite isotropical standard material. The direction of g-shift for $H//a$-axis and $H//c$-axis are opposite to that for $H//b$-axis. This axial dependence of g-shift in TOV can also be explained by whether the magnetic field is parallel or perpendicular to the magnetic plane, as found in the 2DHAF compound K_2MnF_4 [69]. The results for the b-axis of TOV show the character expected for the field perpendicular to the 2D magnetic ordering plane, and those for the a- and c-axes do for the field within the plane.

4.3.6 Weak-Ferromagnetism of TOV

In this sub-section, we discuss about the possibility of the D-M interaction on the weak ferromagnetism of TOV. The D-M interaction is of the order of

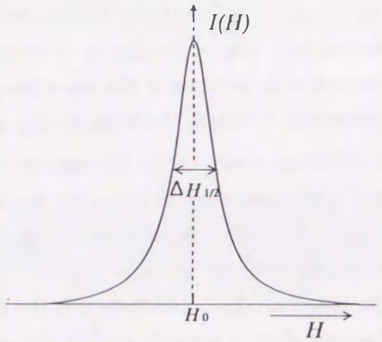

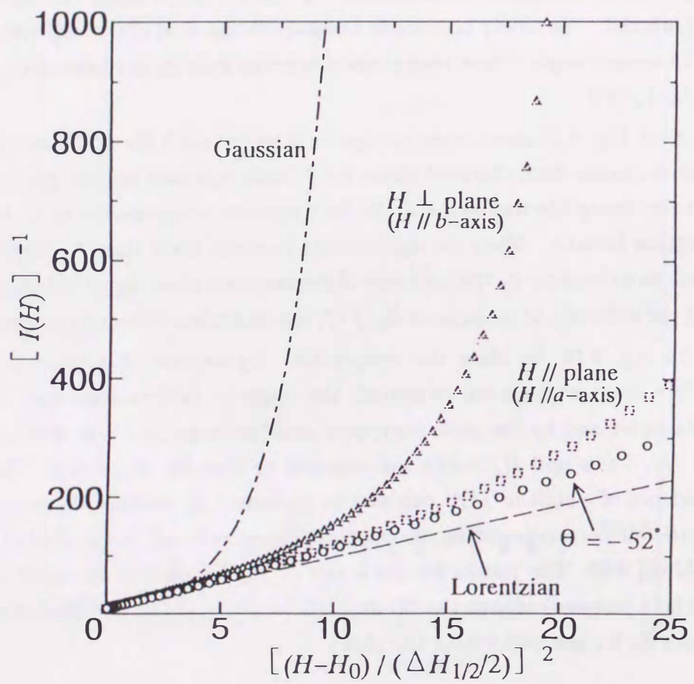

Figure 4.14: Angular dependence of the EPR lineshape of TOV in $H//ab$-plane. θ is the angle between the b-axis and H, as used in Fig.4.12. o: θ = -52°, □: $H//a$-axis, and △: $H//b$-axis.

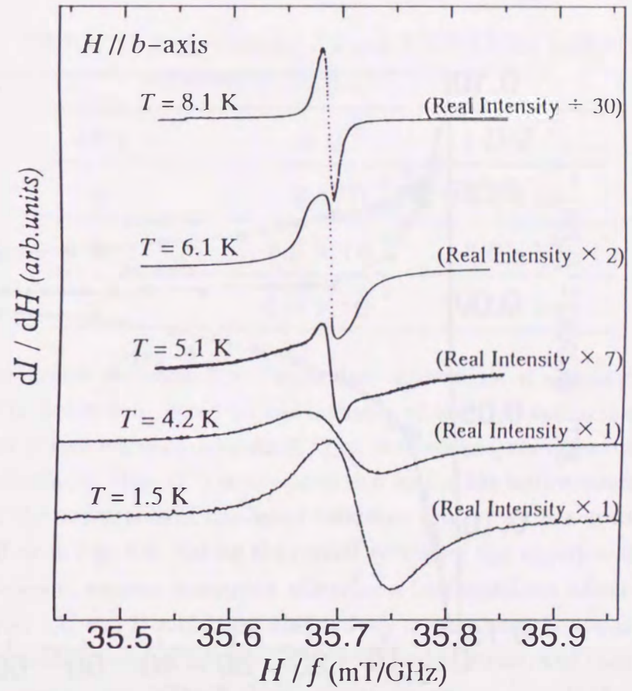

Figure 4.15: Temperature dependence of derivative line dI/dH of TOV for $H//b$-axis below 8.1 K.

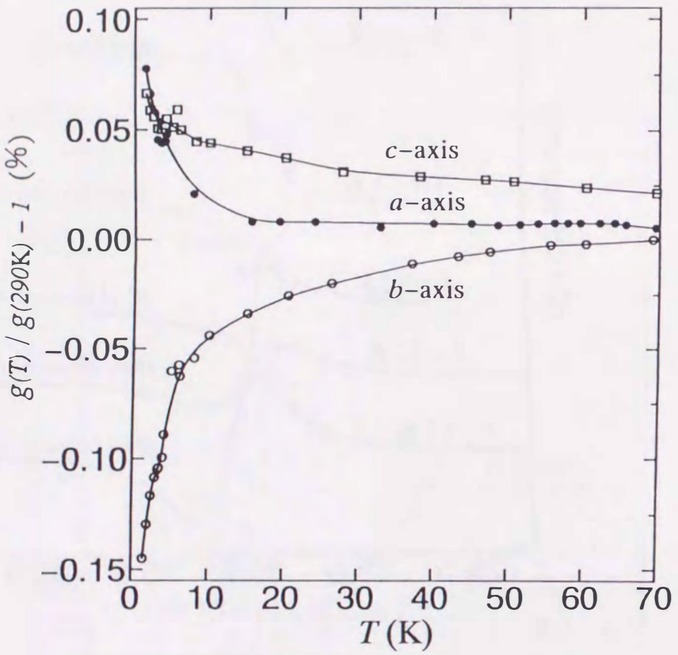

Figure 4.16: Temperature dependence of g-values of TOV for each axis. •: $H//a$-axis, ○: $H//b$-axis, and □: $H//c$-axis.

$$|\frac{D}{2J}| = |\frac{\Delta g}{g_e}| = |\frac{g - g_e}{g_e}| \quad , \tag{4.12}$$

where $g_e = 2.0023$. The values of Δg and $|D/2J|$ in *eq.*4.12 are estimated at 2.0 K as in Table.1. Above value of $|D/2J|$ seems to be a little smaller than the results $|D/2J| = 9.6 \times 10^{-3}$ evaluated in subsections 4.3.3 and 4.3.4, though the same order of magnitude. We may conclude that the weak ferromagnetic moment of TOV is possible by the D-M interaction with the anisotropy of this magnitude.

TABLE I. The values of Δg and $|D/2J|$ for each axis estimated at 2.0 K.

axis	Δg	$\lvert D/2J \rvert$
a	2.4×10^{-3}	1.2×10^{-3}
b	-1.6×10^{-3}	8.0×10^{-4}
c	8.0×10^{-4}	4.0×10^{-4}

Next, we discuss the anomalous temperature dependence of magnetic susceptibility of TOV below 6 K, based on the interplay of the D-M interaction and the development of spin correlation length $\xi(T)$ on the ac-plane, since the other effects are expected minute. Here $\xi(T)$ is measured in a unit of the lattice constant. First we consider the appearance of the broad maximum around 2.0 K and its decrease below 2.0 K as in Fig. 4.9. Taking the crystal symmetry and experimental results into consideration, we may tentatively introduce a four-sublattice model as shown in Fig. 4.17(a). A- and B-sublattices alternatively locate along the c-axis (see Fig. 4.1(b)). The middle point of S_i^A and S_i^B is the inversion center, and then the D-M interaction cannot occur between them. While, we assume each D-M vector D_{ij}^A and D_{ij}^B between adjacent two spins on the same sublattices. First, we suppose $D_{ij}^A = D_{ij}^B$, though this is not the present case, then the spin arrangement such as Fig. 4.17(b) is stabilized under the following condition on the D-M interaction,

$$D_{ij} \cdot (S_i \times S_j) = D_{ji} \cdot (S_j \times S_i) \quad . \tag{4.13}$$

In this case, the net magnetic moment does not appear. In the case of $D_{ij}^A = -D_{ij}^B$, which is realistic in the TOV crystal with inversion center as mentioned in section 4.2, there remains the canting moments as in Fig. 4.17(c). However, when the system size $\xi(T)$ along the a-axis under the condition of *eq.*4.13 is extended, the net

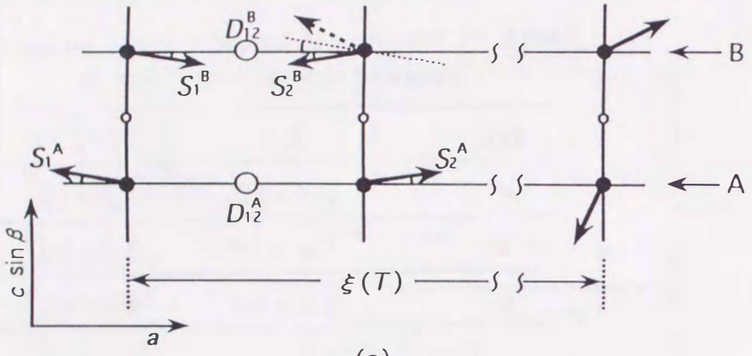

(a)

(b) $D_{12}^{A} = D_{12}^{B}$

(c) $D_{12}^{A} = -D_{12}^{B}$

Figure 4.17: The four-sublattice model with two kinds of D-M vectors on the ac-plane. •: molecule of TOV, ○: inversion center along the c-axis, and ◯: D-M vectors in each sublattice.

moment for each sublattices rotates depending on the canting angle ϕ'. Then the bulk magnetization may become smaller and eventually disappear for $\xi > \xi_c$ where $\xi_c\phi' \cong \pi$, quenching magnetic susceptibility as well. That is, the development of $\xi(T)$ reflects the magnetic susceptibility and/or the magnetic moment. The rounding and decreasing of χ_{ac} around 2.0 K in Fig. 4.9 can be qualitatively explained by above model, where the correlation length is sufficiently long. As the ϕ' is expected much less than 1° as mentioned in the previous subsection 4.3.4, ξ_c may be longer than 100 at these temperatures.

Here, we examine the susceptibility in the critical region just below 6 K, taking the dependence of spin correlation length $\xi(T)$ into consideration.

This anomaly of the susceptibility is relevant to the anisotropy inherent in this system and gives the information about the antiferromagnetic staggered susceptibility as follows.

Generally the staggered susceptibility is regarded as a fictitious quantity in ordinary antiferromagnets. However, in the case with the canting moments caused by the D-M interactions and/or with two kinds of the g-tensor (g_1 and g_2), the observed susceptibility χ_{total} is expressed by the sum of the contributions of the uniform susceptibility $\chi_{uniform}$ and a fraction of the staggered susceptibility $\epsilon\chi_{st}$ ($\epsilon \ll 1$),

$$\chi_{total} = \chi_{uniform} + \epsilon\chi_{st}, \tag{4.14}$$

where $\chi_{uniform}$ and χ_{st} are the corresponding quantities for the non-canted system with the same exchange interaction. In the case of g_1 and g_2 system, ϵ is formalized as a function of anisotropy of the g-tensor $\Delta g/g$ [70]. In 2DHAF the value of χ_{st} itself is much larger than $\chi_{uniform}$, about one order of magnitude at $k_BT/|2J| = 1.0$, for example [55,58]. But it is diminished by the factor ϵ in the canted system. By our EPR experiment for the TOV crystal, we get the value of $\Delta g/g_e$ less than 0.2 % (possible magnitude giving $\phi \cong \Delta g/g_e$). In the region where the temperature is higher than $k_BT/|2J| = 1.0$, χ_{ac} of TOV is described by dominant $\chi_{uniform}$ which is consistent with the high temperature series expansion for $S = 1/2$ 2DHAF as shown in Fig. 4.8. At lower temperatures, however, $\epsilon\chi_{st}$ is expected to overwhelm $\chi_{uniform}$ and diverge for $T \to 0$ K, whereas $\chi_{uniform}$ is small and relatively temperature independent. Then we try to explain the increase of χ_{ac} of TOV with the sum of these contribution below 6 K.

The staggered susceptibility $\chi(T)$ and the spin correlation length $\xi(T)$ near the critical temperature T_c are respectively expressed with each critical index as follows:

$$\chi(T) \propto |\frac{T-T_c}{T_c}|^{-\gamma} \quad , \tag{4.15}$$

$$\xi(T) \propto |\frac{T-T_c}{T_c}|^{-\nu} \quad . \tag{4.16}$$

The validity of the following Fisher's relation,

$$\frac{\gamma}{\nu} = 2 - \eta \quad , \tag{4.17}$$

has been examined for various magnetic system (*e.g.* $\eta = 1/4$ for the Kosterliz-Thouless transition). Theoretically for the 2DHAF with $S = 1/2$, the relation of $\chi(T)$ and $\xi(T)$ is studied by the Monte Carlo method [54]. We analyzed this theoretical results to notice that the value of $\eta \cong 0$ is hold within the error of 7 % in rather wider temperature region such as $0.5 \leq k_B T/|2J| \leq 1.5$, that is $\chi \cong \xi^2$. In the present calculation of χ, we use the following notation of $\xi(T)$ [56], only because of the advantage of its analytic expression with nearly the same value as in ref.54,

$$\xi(T) = C' \frac{exp(2\pi\rho_s/k_B T)}{1 + k_B T/2\pi\rho_s}, \tag{4.18}$$

where $2\pi\rho_s/k_B T = 0.8145\ |2J|$ and C' being a constant. The system size or spin correlation length is evaluated theoretically, for 2DHAF, which gives $\xi(T) \cong 46$ lattice sites at $k_B T/|2J| \cong 0.23$, which corresponding to $T \cong 2.0$ K for $J/k_B =$ -4.5 K. In order to see these relations hold in the present 2D system, we show the semi-log plot of χ_{ac} below 10 K in Fig. 4.18, where we plotted the analytic line (a) of $\chi_{uniform}$ for $J/k_B =$ -4.5 K by the Monte Carlo simulation [53] and three analytic lines (b) of $\epsilon\chi_{st} = \epsilon\xi^2$ for $J/k_B =$ -4.5 $\pm$ 1.5 K and $\epsilon \cong 1.16 \times 10^{-3}$. Here we used the results by the susceptometer in the temperature region above 2.1 K, because the data measured simultaneously with the heat capacity lacks accuracy at higher temperatures. Our experimental results of χ_{ac} above 6 K is reproduced by $\chi_{uniform}$ of the high temperature series expansion as in subsection 4.3.2. Below 6 K, however, we can not explain the rapid growth of χ_{ac} with these equations, though the quantitative explanation with above model may be possible. Rather we can explain the increase of χ_{ac} as the crossover effect for two-dimensional Heisenberg (2DH) system to two-dimensional Ising (2DI) system, whose behavior is reproduced by the analytic result (c) of *eq*.4.15 with $T_c = 4.8$ K and the critical index $\gamma \cong 1.75$ for the 2DI model. The critical temperature region is rather narrow as seen in Fig. 4.19.

This is due to the rounding of χ_{ac} related with the rotation of net moments for the longer $\xi(T)$ as mentioned just above. The results are compared with the crossover

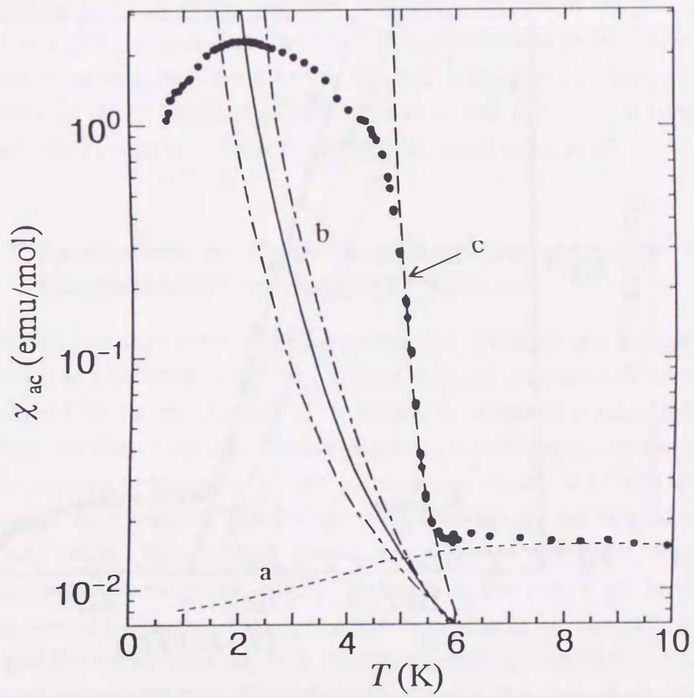

Figure 4.18: The semi-log plot of χ_{ac} of TOV versus T below 10 K. (•): Experimental results of χ_{ac}, (a): $\chi_{uniform}$ for $J/k_B =$ -4.5 K by the Monte Carlo simulation [53], (b): $\epsilon\chi_{st} = \epsilon\xi^2$ for the 2DHAF with $J/k_B =$ -4.5 $\pm$ 1.5 K and $\epsilon \cong 1.16 \times 10^{-3}$, and (c): $\chi \propto |(T - T_c)/T_c|^{-\gamma}$ for the 2D Ising system with $T_c = 4.8$ K and $\gamma = 1.75$.

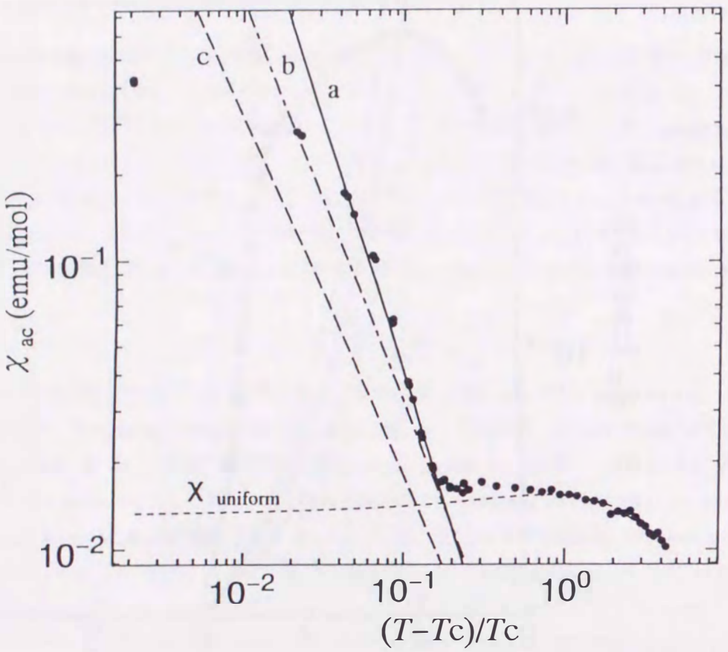

Figure 4.19: The log-log plot of χ_{ac} of TOV versus $|T - T_c|/T_c$ above T_c. The three lines (a, b and c) show χ versus $|(T - T_c)/T_c|^{-\gamma}$ with $T_c = 4.8$ K for $\gamma = 1.75$ (2DI), 1.4 (3DH) and 1.25 (3DI), respectively.

to the three-dimensional (3D) systems, in which $\gamma \cong 1.4$ for the Heisenberg and $\gamma \cong 1.25$ for the Ising systems. If the crossover is one to 3D system at T_c, the interplane exchange interaction J', which is expressed in the molecular field theory as,

$$k_B T_c \simeq 2|J'|S^2 \xi_{2D}^2(T_c), \tag{4.19}$$

is estimated to be $|J'/J| \cong 0.2$, giving an expectation of a distinct λ-peak in the heat capacity at T_c. In reality, any trace of it cannot be seen in Fig. 4.5. Then the spin-dimensional crossover from 2DH to 2DI is considerable in this system. This Ising anisotropy may be relevant to the existence of Δg shown in Table.1. Here we comment that the frequency ($5 \sim 1000$ Hz) and ac-field ($0.6 \sim 10$ Oe) dependence of χ_{ac} around T_c were not serious to change the critical index at all.

4.3.7 Limitation of Bulk-Ferromagnetic Moment in the Canted Antiferromagnetic System.

Although the appearance of bulk-ferromagnetic moments are realized in such compounds as mentioned in section 1.1, their ordering temperatures are relatively small, $T_c = 1.5K$ for example [18]. This implies the difficulty of introducing direct bulk-ferromagnetism in genuine organic magnets. In this chapter, we have revealed that the ordering temperature of weak ferromagnetic system of TOV is about 5 K, fairly higher than those of bulk-ferromagnets, although its net magnetic moment M_0 is very small. This ordering temperature is related with the strength of antiferromagnetic interaction ($T_c \propto |J|$). Generally in the case of antiferromagnetic systems, we can realize rather stronger interactions than in ferromagnetic cases, and hence find the net moment M_0 with the higher ordering temperature T_c (or J) in the canted antiferromagnets. From the inset in Fig. 4.11 and eqs.4.10 and 4.12, we have

$$\begin{aligned} M_0 = 2M_s \sin\phi &\simeq 2M_s \cdot |D/2J| = M_s|D/J| \ , \\ M_0 T_c &- M_s|D| \ , \end{aligned} \tag{4.20}$$

where M_s is the saturated sublattice magnetization ($M_s = Ng\mu_B S$). When the magnitude of $|D|$ is given, the right-hand side of eq.4.20 becomes a constant, giving a limitation for magnitudes of T_c and M_0. If we want to have the higher T_c, the smaller moment we have in this canting mechanism. Otherwise we have to make $|D|$ itself larger, although it seems to be difficult to introduce large $|D|$ in genuine organic compounds. The magnitude of $|D|$ is derived from the second order of perturbation

including the spin-orbital interaction $\lambda \boldsymbol{L} \cdot \boldsymbol{S}$. We may suggest to introduce some rare earth elements with larger $\lambda \boldsymbol{L} \cdot \boldsymbol{S}$ interaction in organic compounds for realizing effective canted moments.

Recently a few weak-ferromagnets with higher ordering temperatures have been reported [†]. It is interesting to check the limitation given here in these compounds.

4.4 Conclusion

We determined the low temperature magnetic properties of 1.3.5-Triphenyl-6-Oxoverdazyl (TOV) by the experiments of heat capacity, magnetic susceptibility, magnetization and EPR. We have revealed that the experimental results of heat capacity and magnetic susceptibility above T_c is described by an $S = 1/2$ two-dimensional Heisenberg antiferromagnet with an effective exchange interaction J/k_B = -4.5 ± 0.2 K. We observed the feature of the two-dimensional system also in the measurement of EPR. In the measurements of the magnetic susceptibility and the magnetization below 6 K, the weak ferromagnetic properties is confirmed, in which the Dzyaloshinsky-Moriya type anisotropy is assumed and its magnitude is estimated to be $D \cong 1$ kOe. The results of EPR show the anisotropic g-factors along each axis, and this may be the origin of the Dzyaloshinsky-Moriya interaction. The anomalous rounding of the magnetic susceptibility around 2.0 K is explained by a four-sublattice model with two kinds of D-M vectors of opposite sign on the ac-plane, in which the interplay between the development of the net magnetic moment and the spin correlation length was taken into consideration. With the use of the canted weak ferromagnet, the staggered susceptibility for the 2DHAF system is estimated. Especially the rapid growth of magnetic susceptibility just below 6 K is explained with crossover effect from two-dimensional Heisenberg system to two-dimensional Ising system, which will be induced by the above D-M anisotropy. But the anomaly of heat capacity by this anisotropy is not observed. This fact suggests the effect of the anisotropy on the thermal energy for the 2DHAF with $J/k_B \cong$ -4.5 K is negligibly small.

[†]T.Sugimoto *et al.* has been reported that the weak-ferromagnetic behavior has been observed in some TCNQ salts at room temperature [71]. F.Palacio *et al.* reported a sulfur-nitrogen radical (β-phase p-NCC_6F_4CNSSN) with a spontaneous magnetization at 36 K at the Vth International Conference on Molecular-Based Magnets (Osaka, Japan, July, 1996) [72]. Here we define T_c as the temperature at which M_0 appears. The highest T_c in the verdazyl series is 5.4 K of TOV [63,73].